

Spectral function of holes in the Emery model

P. Unger and P. Fulde

*Max-Planck-Institut für Festkörperforschung
70569 Stuttgart, Germany*

(Received 21 May 1993)

We calculate the single-particle excitation spectrum of holes in the Emery model thereby extending and improving previous calculations. The system is considered at half filling ($n_h = 1$, one hole per CuO_2 unit) and for hole doping, where the on-site hole-hole repulsions are kept finite. A paramagnetic form of the ground state is used. For the determination of the retarded Green's functions of copper and oxygen holes, the projection technique is applied solving the resulting equations of motions self-consistently. At half filling, the excitation spectrum exhibits a charge-transfer gap bounded by Zhang-Rice singlet states and the upper Hubbard band. Upon hole doping the flat singlet band crosses the Fermi level giving rise to a large Fermi surface at a hole concentration of $n_h = 1.25$. Moreover, spectral weight is shifted from the upper Hubbard band to the states near the Fermi energy. The calculated spectral densities, the singlet dispersion for the doped system, and the transfer of spectral weight are in good quantitative agreement with exact diagonalization results for 2×2 CuO_2 cluster.

I. INTRODUCTION

A satisfactory theoretical description of single-particle excitations in the normal state of cuprate superconductors is still a challenging problem. Their surprising experimental properties as well as the theoretical intricacies originate from the strong Coulomb interaction between the charge carriers in the copper-oxygen planes, the characteristic structural unit of this class of materials. Due to the strong Coulomb repulsion U_d , which two holes on a copper site experience La_2CuO_4 for example is a semiconductor with a charge-transfer gap, whereas conventional band-structure calculations predict metallic behavior.

An adequate treatment of strongly correlated charge carriers remains a difficult task even if the physics of real solids is condensed into simplified Hamiltonians. In the case of high- T_c cuprates the Emery model,¹ which is a three-band Hubbard model on a two-dimensional square lattice provides a good starting point for a theoretical analysis. The parameters of the model Hamiltonian²⁻⁴ can be derived from band-structure calculations^{5,6} or quantum chemical approaches.^{7,8} Its ground-state properties and excitation spectrum have been intensively studied by numerical methods like exact diagonalization of small clusters⁹⁻¹⁸ or Monte Carlo techniques.¹⁹⁻²¹ Furthermore, the Emery model formed the starting point of numerous analytical approaches for cuprate superconductors. Several authors applied the slave-boson formalism²²⁻²⁷ or used the equation-of-motion method.^{28,29} In other works the Hamiltonian of the Emery model was further simplified by canonical transformations.³⁰⁻³² This way one is finally led to the t - J model,³³ which seems to describe accurately the low-energy excitations of the Emery model. Finally the projection technique, which will be used in this work, has already been applied to determine the spectral densities for copper and oxygen holes (Refs. 34-37).

The theoretical results must be compared with photoe-

mission (PES) and inverse photoemission spectroscopy (IPES) measurements. For example, angular resolved PES on $\text{Bi}_2\text{Sr}_2\text{CaCu}_2\text{O}_8$,³⁸⁻⁴⁰ a self-doped material, give a rather flat band, which is crossing the Fermi level and is also detected above the Fermi energy by IPES.⁴¹ In $\text{YBa}_2\text{Cu}_3\text{O}_{7-y}$, doping with holes ($0.1 \leq y \leq 0.7$) leads to a remarkable increase in intensity of these low-energy excitations.⁴² Additional information is obtained from O $1s$ absorption edge measurements, where a simultaneous decrease in spectral weight of states, which are about 2 eV above the Fermi energy, is observed.^{43,44}

As mentioned before, due to strong Coulomb interactions several of the high- T_c compounds exhibit an energy gap at half filling of about 1.5 – 2 eV. However, if the systems are far from half filling the measured Fermi volume⁴⁵⁻⁴⁷ does not correspond to the number of additional charge carriers introduced by doping but rather to the total number of electrons in the system, in accordance with the picture of independent quasiparticles and with Luttinger's theorem.⁴⁸ But the details of the transition remain a puzzle, i.e., from an insulating state without a Fermi surface at half filling to a metal with a large Fermi surface as a consequence of doping.

In this paper we present a calculation of the single-particle spectral densities of copper and oxygen holes in the Emery model. We consider the system at half filling and for low levels of hole doping and assume a paramagnetic ground state. The long-range antiferromagnetic order present in a cuprate such as $\text{La}_{2-x}\text{Sr}_x\text{CuO}_4$ at half filling ($x = 0$) is rapidly destroyed by hole doping. For doping concentrations of 20%, the ground state is paramagnetic although with strong short-range antiferromagnetic correlations. The retarded Green's functions will be determined by the projection technique solving the resulting equations of motion self-consistently. The present approach extends and completes our previous study of the excitation spectrum,³⁷ where we started from a copper spin system with long-range antiferromag-

netic order and made a perturbational ansatz for the ground-state wave function.

As before, we find an insulator at half filling, which turns into a metal if the system is doped with holes. For a hole concentration of $n_h = 1.25$ a large Fermi surface is obtained lying close to the experimental results. Additionally, the dispersion of the band crossing the Fermi level coincides with angle-resolved photoemission data (ARPES). As a consequence of hole doping, spectral weight is shifted from the upper Hubbard band to states near the Fermi energy. The effect is in agreement with exact diagonalization studies. The accuracy of our approach is tested for a 2×2 CuO₂ cluster by comparing the excitation spectrum to exact results.

We start with the introduction of the model Hamiltonian in Sec. II and continue by explaining the formalism of the self-consistent projection technique (Sec. III). The search for relevant projection operators is the decisive step in the calculations. We discuss our choice in detail in Sec. IV. Thereafter, the resulting spectra are presented. We begin with a comparison to the results of exact diagonalization (Sec. V). Then we analyze in Sec. VI the results for the Emery model, in particular the peak structure, consider the shift of spectral weight (Sec. VII) and finally the doping dependence of the Fermi surface (Sec. VIII). Several details of the calculation are presented in the Appendix.

II. THE MODEL

The Emery model describes the motion of holes in the copper-oxygen planes of the high- T_c materials. Three types of local states form the basis of the square lattice, i.e., a Cu $3d_{x^2-y^2}$, a O $2p_x$, and a O $2p_y$ orbital (see Fig. 1). A hole can hop from an oxygen site to the nearest copper orbitals via a matrix element t_{pd} and to the nearest oxygen orbitals via the hopping term t_{pp} . On a copper site, two holes experience a Coulomb repulsion U_d and on an oxygen site a repulsion U_p . The orbital energies for Cu $3d_{x^2-y^2}$ and $2p_{x(y)}$ are denoted by e_d and e_p , respectively. They are separated by the charge-transfer energy $\Delta = e_p - e_d$. Using a basis of oxygen orbitals, which is diagonal with respect to oxygen-oxygen hopping t_{pp} the

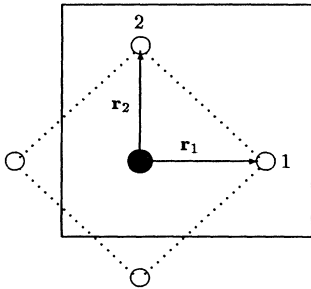


FIG. 1. Unit cell of the copper-oxygen plane: Two oxygen $2p$ orbitals (open circles) and one copper $3d$ orbital (black dot) form the basis. The dotted lines connect the four oxygen orbitals of a CuO₄ plaquette.

Hamiltonian of the Emery model can be written as

$$H = \sum_{m\mathbf{k}\sigma} \epsilon_{m\mathbf{k}} c_{m\mathbf{k}\sigma}^\dagger c_{m\mathbf{k}\sigma} + U_p \sum_{m\mathbf{k}} \bar{c}_{m\mathbf{k}\uparrow}^\dagger \bar{c}_{m\mathbf{k}\uparrow} + e_d \sum_{\mathbf{k}\sigma} d_{\mathbf{k}\sigma}^\dagger d_{\mathbf{k}\sigma} + U_d \sum_{\mathbf{k}} \bar{d}_{\mathbf{k}\uparrow}^\dagger \bar{d}_{\mathbf{k}\uparrow} + 2t_{pd} \sum_{m\mathbf{k}\sigma} \left(\phi_{m\mathbf{k}} c_{m\mathbf{k}\sigma}^\dagger d_{\mathbf{k}\sigma} + \phi_{m\mathbf{k}}^* d_{\mathbf{k}\sigma}^\dagger c_{m\mathbf{k}\sigma} \right). \quad (1)$$

The operator $c_{m\mathbf{k}\sigma}^\dagger$ creates a hole in oxygen band m with wave vector \mathbf{k} and spin σ . A copper hole is generated by $d_{\mathbf{k}\sigma}^\dagger$. The operator $\bar{d}_{\mathbf{k}\uparrow}^\dagger$ is the Fourier transform of the local operator $\bar{d}_{I\uparrow}^\dagger = d_{I\uparrow}^\dagger n_{I\downarrow}$ ($n_{I\downarrow} = d_{I\downarrow}^\dagger d_{I\downarrow}$), where I is the cell index. According to this definition $\bar{d}_{I\uparrow}^\dagger$ creates exclusively doubly occupied Cu $3d_{x^2-y^2}$ orbitals. In the same way the operator $\bar{c}_{m\mathbf{k}\uparrow}^\dagger$ acts on oxygen sites.

The oxygen-oxygen hopping t_{pp} leads to two tight-binding bands $m=1, 2$ with the dispersion relations

$$\epsilon_{m\mathbf{k}} = e_p \pm 2t_{pp} \{ \cos[\mathbf{k}(\mathbf{r}_1 + \mathbf{r}_2)] - \cos[\mathbf{k}(\mathbf{r}_2 - \mathbf{r}_1)] \}. \quad (2)$$

The vectors $\mathbf{r}_1, \mathbf{r}_2$ are shown in Fig. 1. Due to the different orientations of the O $2p_{x(y)}$ orbitals the sign of the nearest-neighbor oxygen-oxygen hopping depends on the direction. It is positive in the directions $\mathbf{r}_1 + \mathbf{r}_2, -(\mathbf{r}_1 + \mathbf{r}_2)$, and negative for $\mathbf{r}_1 - \mathbf{r}_2, \mathbf{r}_2 - \mathbf{r}_1$. The copper and oxygen systems are connected by the hopping term t_{pd} . The corresponding phase factor $\phi_{m\mathbf{k}}, m=1, 2$, is of the form

$$\phi_{m\mathbf{k}} = -i2^{-\frac{1}{2}} [\sin(\mathbf{k}\mathbf{r}_1) \pm \sin(\mathbf{k}\mathbf{r}_2)]. \quad (3)$$

The hopping matrix element t_{pd} is negative for copper-oxygen jumps within a unit cell, and positive for jumps to neighboring cells.

General agreement has been achieved with respect to the values of the parameter set in cuprate superconductors. Hybertsen *et al.*² for example, give the values $U_d = 10.5$ eV, $U_p = 4.0$ eV, $\Delta = 3.6$ eV, $t_{pd} = 1.3$ eV, and $t_{pp} = 0.65$ eV. These results have been extracted from band-structure calculations.

It is useful to introduce a linear combination of oxygen orbitals that possesses the same symmetry on a CuO₄ plaquette as the t_{pd} -matrix elements and that is called the symmetric one:

$$p_{\mathbf{k}\sigma}^\dagger = \sum_m \phi_{m\mathbf{k}} c_{m\mathbf{k}\sigma}^\dagger. \quad (4)$$

Only this linear combination of oxygen states with wave vector \mathbf{k} couples to the copper system as can be seen from Eq. (1).

III. PROJECTION TECHNIQUE

The one-particle spectrum of holes in the Emery model can be calculated by considering the corresponding retarded Green's function. For two arbitrary operators $A_m(\mathbf{k}), A_n(\mathbf{k})$ it is defined as

$$G_{mn}(\mathbf{k}, t) = -i\theta(t) \langle [A_m^\dagger(\mathbf{k}, t), A_n(\mathbf{k})]_+ \rangle. \quad (5)$$

The expectation value denotes the thermal average over a grand canonical ensemble:

$$\langle A \rangle = \frac{1}{Z} \text{Tr} e^{-\beta(H-\mu N)} A, \quad Z = \text{Tr} e^{-\beta(H-\mu N)}. \quad (6)$$

Here, Tr implies taking the trace of an operator, N is the electron number operator, $\beta = (kT)^{-1}$ is an inverse temperature, and μ represents the chemical potential. The time dependence of the operator $A_m^\dagger(\mathbf{k}, t)$ is given by

$$A_m^\dagger(\mathbf{k}, t) = e^{it(H-\mu N)} A_m^\dagger(\mathbf{k}) e^{-it(H-\mu N)}. \quad (7)$$

The function $\theta(t)$ equals 1 for $t > 0$ and 0 for $t < 0$.

After a Laplace transform the frequency-dependent Green's function $G_{mn}(\mathbf{k}, \omega)$ may be written in the form

$$G_{mn}(\mathbf{k}, \omega) = \left(A_m^\dagger(\mathbf{k}) \left| \frac{1}{\omega - \mathcal{L}} A_n(\mathbf{k}) \right. \right). \quad (8)$$

Thereby, the anticommutator has been absorbed in the definition of the parentheses, i.e., $(A^\dagger|B) = \langle [A^\dagger, B]_+ \rangle$. Furthermore, the Liouvillean \mathcal{L} is a superoperator, which acts on an operator A according to $\mathcal{L}A = [H, A]_-$.

Equation (8) is in a proper form to be evaluated by the partitioning or projection technique.^{49,50} The basic principle of this approach is to divide the total space of the operators, i.e., the Liouville space, into a relevant and an irrelevant part. Only the relevant part is kept, while the irrelevant part is neglected. Let us assume that the relevant subspace is spanned by the set of operators $\mathcal{R} = \{A_1(\mathbf{k}), \dots, A_M(\mathbf{k})\}$. The following projection equation is found for the retarded Green's function matrix \underline{G} of the operators $\{A_1(\mathbf{k}), \dots, A_M(\mathbf{k})\}$ if the coupling of \underline{G} to the irrelevant part of the Liouville space is omitted (see, for example, Ref. 51):

$$\underline{G} = \underline{X} [\omega \cdot \underline{X} - \underline{F}]^{-1} \underline{X}. \quad (9)$$

The susceptibility matrix \underline{X} and the frequency matrix \underline{F} are defined as

$$X_{mn}(\mathbf{k}) = (A_m^\dagger(\mathbf{k}) | A_n(\mathbf{k})), \quad (10)$$

$$F_{mn}(\mathbf{k}) = (A_m^\dagger(\mathbf{k}) | \mathcal{L} A_n(\mathbf{k})). \quad (11)$$

Provided that all static quantities appearing in \underline{X} and \underline{F} are known, the dynamics within \mathcal{R} is treated exactly.

From the retarded Green's functions $G_{mn}(\mathbf{k}, \omega)$ the corresponding spectral function $S_{mn}(\mathbf{k}, \omega)$ is obtained by using the familiar relation

$$S_{mn}(\mathbf{k}, \omega) = -\frac{1}{\pi} \lim_{\eta \rightarrow 0^+} \text{Im}[G_{mn}(\mathbf{k}, \omega + i\eta)]. \quad (12)$$

The spectral functions are the quantities we are finally interested in, since they can be compared with measured photoemission and inverse photoemission spectra of the high- T_c materials. As will be shown in the next section, the matrix elements of \underline{X} and \underline{F} depend upon static expectation values of the form $\langle A_m(\mathbf{k}) A_n^\dagger(\mathbf{k}) \rangle$, i.e., expectation values within the relevant set \mathcal{R} of the Liouville space. On the other hand, these static expressions are obtained by a frequency integration over the corresponding spectral function

$$\langle A_m(\mathbf{k}) A_n^\dagger(\mathbf{k}) \rangle = \int_{-\infty}^{\infty} d\omega S_{nm}(\mathbf{k}, \omega) f(\omega), \quad (13)$$

where $f(\omega) = [e^{\beta(\omega-\mu)} + 1]^{-1}$ is the Fermi distribution. Starting from an initial set of static expectation values $\langle A_m(\mathbf{k}) A_n^\dagger(\mathbf{k}) \rangle$ the frequency and susceptibility matrices can be calculated. After solving the matrix equation (9) the retarded Green's functions $G_{mn}(\mathbf{k}, \omega)$, the spectral functions $S_{mn}(\mathbf{k}, \omega)$ and finally new values for $\langle A_m(\mathbf{k}) A_n^\dagger(\mathbf{k}) \rangle$ are obtained. The described loop has to be continued until self-consistency is achieved. Along these lines accurate excitation spectra, as well as precise ground-state expectation values are determined without making an explicit ansatz for the ground-state wave function of the system. The self-consistent procedure forms the main difference to our former usage of the projection technique,³⁷ where we applied degenerate perturbation theory to construct a ground-state wave function with antiferromagnetic long-range order.

The projection equation (9) can also be derived by considering the equations of motion for the retarded Green's functions. In that case one can identify the projection onto a relevant subspace with a truncation of the hierarchy of differential equations at a certain stage. Although the projection method is more general, there are indeed strong similarities to the conventional equation-of-motion method. An advantage of the projection scheme presented above is the inherent hermiticity of \underline{F} and \underline{X} together with the positive definiteness of the susceptibility matrix. If the commutators of operators with the Hamiltonian are approximated directly, as often is done in the equation-of-motion method, the mentioned characteristics of the corresponding frequency and susceptibility matrices may be violated leading to spectral densities with negative weight, for example.

IV. RELEVANT OPERATORS

For a successful application of the projection technique the proper choice of the relevant subspace is essential. In the case of holes in the Emery model a set of nine operators $A_n(\mathbf{k})$ for each \mathbf{k} value turns out to be sufficient for an accurate description of the excitation spectrum:

$$A_p(m, \mathbf{k}) = c_{m\mathbf{k}\uparrow}^\dagger, \quad A_d(\mathbf{k}) = d_{\mathbf{k}\uparrow}^\dagger, \quad (14)$$

$$A_{\bar{p}}(m, \mathbf{k}) = \bar{c}_{m\mathbf{k}\uparrow}^\dagger, \quad A_{\bar{d}}(\mathbf{k}) = \bar{d}_{\mathbf{k}\uparrow}^\dagger, \quad (15)$$

$$A_s(\mathbf{k}) = \frac{1}{\sqrt{N}} \sum_{\mathbf{q}} p_{\mathbf{q}\downarrow}^\dagger S_{(\mathbf{k}-\mathbf{q})}^+, \quad (16)$$

$$A_c(\mathbf{k}) = \frac{1}{\sqrt{N}} \sum_{\mathbf{q}} p_{\mathbf{q}\uparrow}^\dagger n_{(\mathbf{k}-\mathbf{q})\downarrow}, \quad (17)$$

$$A_t(\mathbf{k}) = \frac{1}{N} \sum_{\mathbf{q}_1 \mathbf{q}_2} p_{\mathbf{q}_1\uparrow}^\dagger p_{\mathbf{q}_2\downarrow}^\dagger d_{(\mathbf{q}_1+\mathbf{q}_2-\mathbf{k})\downarrow}. \quad (18)$$

The operator $S_{\mathbf{k}}^+$ is the Fourier transform of the local spin-flip operator on a copper site I , $S_I^+ = d_{I\uparrow}^\dagger d_{I\downarrow}$. The corresponding quantity for the copper density operator $n_{I\downarrow}$ is denoted by $n_{\mathbf{k}\downarrow}$. As before, $m = 1, 2$ denotes the band index and N is the number of unit cells in the system.

The operators A_p , A_d form the starting point for the construction of the relevant subspace, since we are finally interested in the spectral densities of copper and oxygen holes. In principle, all other operators are found by considering the series $\mathcal{L}A_d$, \mathcal{L}^2A_d , \mathcal{L}^3A_d , etc., or $\mathcal{L}A_p$, \mathcal{L}^2A_p , \mathcal{L}^3A_p , and so on. As we follow these lines we successively create all operators which couple to the initial configurations.

If the Liouville operator is applied to the creation operators for copper and oxygen holes, the Coulomb interactions U_d and U_p introduce new operators $A_{\bar{d}}$ and $A_{\bar{p}}$:

$$\mathcal{L} d_{\mathbf{k}\uparrow}^\dagger = e_d d_{\mathbf{k}\uparrow}^\dagger + 2t_{pd} p_{\mathbf{k}\uparrow}^\dagger + U_d \bar{d}_{\mathbf{k}\uparrow}^\dagger, \quad (19)$$

$$\mathcal{L} c_{m\mathbf{k}\uparrow}^\dagger = \epsilon_{m\mathbf{k}} c_{m\mathbf{k}\uparrow}^\dagger + 2t_{pd} \phi_{m\mathbf{k}}^* d_{\mathbf{k}\uparrow}^\dagger + U_p \bar{c}_{m\mathbf{k}\uparrow}^\dagger. \quad (20)$$

As described in the preceding section, the operators $\bar{d}_{\mathbf{k}\uparrow}^\dagger$, $\bar{c}_{m\mathbf{k}\uparrow}^\dagger$ create exclusively doubly occupied copper and oxygen sites, respectively. With the help of the operators A_p , $A_{\bar{p}}$, A_d , and $A_{\bar{d}}$, single and double occupation can be distinguished, thereby taking into account the effect of Coulomb repulsion from an atomic point of view. A self-consistent solution within this operator space leads to the well-known Hubbard I approach⁵² if the frequency matrix is approximated in a certain way (for details see the Appendix). The Hartree-Fock approximation is obtained if we restrict ourselves to the minimal operator space A_p and A_d .

In the Emery model, the projection onto single and double occupancy is incapable of reproducing the essential features of its excitation spectrum. This fact is immediately seen, if one considers the problem of two holes on a single CuO_4 plaquette, which can be solved exactly. The simple model contains in a nutshell the basic ingredients of the strongly correlated three-band system. One finds the ground state to be a linear combination of $p_\uparrow^\dagger p_\downarrow^\dagger | \rangle$, $d_\uparrow^\dagger d_\downarrow^\dagger | \rangle$, and the singlet $s^\dagger | \rangle = 2^{-\frac{1}{2}} (p_\uparrow^\dagger d_\downarrow^\dagger - p_\downarrow^\dagger d_\uparrow^\dagger) | \rangle$, where $| \rangle$ denotes the vacuum. This singlet state is separated from the higher-lying triplet state $t^\dagger | \rangle = 2^{-\frac{1}{2}} (p_\uparrow^\dagger d_\uparrow^\dagger + p_\downarrow^\dagger d_\downarrow^\dagger) | \rangle$ by an energy difference of approximately $8t_{pd}^2/\Delta$. The importance of the singlet formation for the low-lying excitations in the Emery model was first recognized by Zhang and Rice³³ and has been confirmed by exact diagonalization studies of 2×2 CuO_2 cluster.⁹ For that reason an acceptable set of relevant operators must at least be capable of creating locally not only the states $p_\uparrow^\dagger p_\downarrow^\dagger | \rangle$, $d_\uparrow^\dagger d_\downarrow^\dagger | \rangle$, but also $p_\uparrow^\dagger d_\downarrow^\dagger | \rangle$ and $p_\downarrow^\dagger d_\uparrow^\dagger | \rangle$.

Operators fulfilling the required properties are generated when \mathcal{L} acts on $\bar{d}_{\mathbf{k}\uparrow}^\dagger$:

$$\begin{aligned} \mathcal{L} \bar{d}_{\mathbf{k}\uparrow}^\dagger = & (e_d + U_d) \bar{d}_{\mathbf{k}\uparrow}^\dagger - \frac{2t_{pd}}{N} \sum_{\mathbf{q}_1 \mathbf{q}_2} d_{\mathbf{q}_2\uparrow}^\dagger d_{(\mathbf{k}+\mathbf{q}_1-\mathbf{q}_2)\downarrow}^\dagger p_{\mathbf{q}_1\downarrow} \\ & - \frac{2t_{pd}}{\sqrt{N}} \sum_{\mathbf{q}} p_{\mathbf{q}\downarrow}^\dagger S_{(\mathbf{k}-\mathbf{q})}^+ + \frac{2t_{pd}}{\sqrt{N}} \sum_{\mathbf{q}} p_{\mathbf{q}\uparrow}^\dagger n_{(\mathbf{k}-\mathbf{q})\downarrow}. \end{aligned} \quad (21)$$

The third term on the right-hand side of Eq. (21) is the spin-flip operator A_s and the fourth the charge-density operator A_c . Through a t_{pd} hopping process the copper hole $\bar{d}_{\mathbf{k}\uparrow}^\dagger$ on a doubly occupied site turns into a sym-

metric oxygen hole with up or down spin, accompanied by a density or spinflip excitation in the copper system. On a CuO_4 plaquette, the introduced operators generate just the configurations we need to form local singlet and triplet states, since

$$A_s(\mathbf{k}) = \frac{1}{\sqrt{N}} \sum_I e^{-i\mathbf{k}\mathbf{R}_I} p_{I\downarrow}^\dagger S_I^+, \quad (22)$$

$$A_c(\mathbf{k}) = \frac{1}{\sqrt{N}} \sum_I e^{-i\mathbf{k}\mathbf{R}_I} p_{I\uparrow}^\dagger n_{I\downarrow}, \quad (23)$$

where \mathbf{R}_I is a lattice vector pointing to cell I .

Figure 2 shows the two basic processes on a CuO_4 plaquette connecting the configuration $p_\uparrow^\dagger d_\downarrow^\dagger$ with $p_\downarrow^\dagger d_\uparrow^\dagger$. In Fig. 2(a) the intermediate state is a doubly occupied copper site, which can be created by the operator $A_{\bar{d}}$. In contrast to that, two oxygen holes surround an empty copper site in process 2(b). The corresponding configuration is produced by the charge-transfer operator

$$A_t(\mathbf{k}) = \frac{1}{\sqrt{N}} \sum_I e^{-i\mathbf{k}\mathbf{R}_I} p_{I\uparrow}^\dagger p_{I\downarrow}^\dagger d_{I\downarrow}. \quad (24)$$

This completes the choice of the relevant set \mathcal{R} . The transfer operator A_t is generated by $\mathcal{L}A_s$ as well as by $\mathcal{L}A_c$. In the limit $U_d \rightarrow \infty$ the binding energy of the local singlet is exclusively a consequence of including A_t , since double occupancy is completely suppressed in that case. Note, that the oxygen operators $\bar{c}_{m\mathbf{k}\uparrow}^\dagger$ cannot replace A_t . There is no singlet binding energy in the infinite U_d limit if the charge-transfer operator is omitted from the relevant set \mathcal{R} .

The excitation spectra presented in the next sections have been determined with the nine relevant operators introduced above. One could certainly include additional operators by considering higher powers of \mathcal{L} . But their effect on the peak positions and intensities are expected to be small on an energy scale of the order of a few tenths of an electron volt, since our calculated spectra already reproduce the exact results for a 2×2 CuO_2 cluster quite accurately. One could also think of taking operators into account generated by $\mathcal{L}\bar{c}_{m\mathbf{k}\uparrow}^\dagger$. However, due to the low

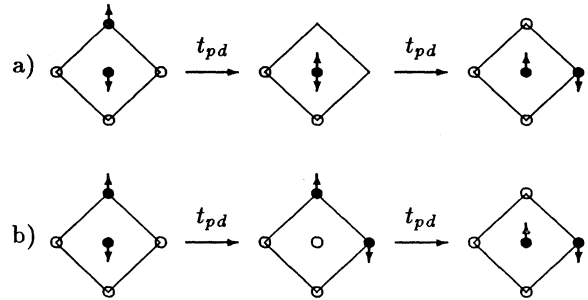


FIG. 2. Two processes, which provide for the formation of singlet and triplet states of two holes (black dots) with opposite spins on a CuO_4 plaquette. In (a) a doubly occupied copper site is created in the intermediate step. In (b) the copper site remains unoccupied (open circle) after the first copper-oxygen hopping process t_{pd} .

oxygen hole-occupation number and the relatively small value of U_p , the influence of the Coulomb repulsion within oxygen sites is of slight importance. This point has been confirmed by exact diagonalization studies.¹²

After the choice of the relevant subspace the susceptibility and frequency matrices \underline{X} and \underline{F} for the nine operators have to be determined. Due to the restricted size of the relevant set \mathcal{R} their matrix elements also depend upon static expectation values, which cannot be calculated self-consistently within this set. Consequently, one is forced to decompose such static quantities into expectation values, which fit into the set of relevant operators. In general, the Hartree-Fock approximation has been used for this purpose, which consists in the replacement

$$\begin{aligned} \langle c_{l_1\mathbf{q}_1\sigma_1}^\dagger c_{l_2\mathbf{q}_2\sigma_2} c_{l_3\mathbf{q}_3\sigma_3}^\dagger c_{l_4\mathbf{q}_4\sigma_4} \rangle &\approx \langle c_{l_1\mathbf{q}_1\sigma_1}^\dagger c_{l_2\mathbf{q}_2\sigma_2} \rangle \langle c_{l_3\mathbf{q}_3\sigma_3}^\dagger c_{l_4\mathbf{q}_4\sigma_4} \rangle \\ &+ \langle c_{l_1\mathbf{q}_1\sigma_1}^\dagger c_{l_4\mathbf{q}_4\sigma_4} \rangle \langle c_{l_2\mathbf{q}_2\sigma_2} c_{l_3\mathbf{q}_3\sigma_3}^\dagger \rangle. \end{aligned} \quad (25)$$

Assuming that there is spin and momentum uniformity in the ground-state wave function, we put

$$\langle c_{l_1\mathbf{q}_1\sigma_1}^\dagger c_{l_2\mathbf{q}_2\sigma_2} \rangle = \delta_{\sigma_1\sigma_2} \delta_{\mathbf{q}_1\mathbf{q}_2} \langle c_{l_1\mathbf{q}_1\sigma_1}^\dagger c_{l_2\mathbf{q}_2\sigma_2} \rangle. \quad (26)$$

Additionally, we presuppose both spin directions to be symmetric, which is characteristic for a paramagnetic state:

$$\langle c_{l_1\mathbf{q}_1\uparrow}^\dagger c_{l_2\mathbf{q}_2\uparrow} \rangle = \langle c_{l_1\mathbf{q}_1\downarrow}^\dagger c_{l_2\mathbf{q}_2\downarrow} \rangle. \quad (27)$$

To Coulomb matrix elements proportional to U_d a local approximation is applied, i.e., we replace the expression valid for the lattice by the corresponding term for a single CuO_4 plaquette. A local approximation is also used for a certain group of t_{pd} and susceptibility terms. For details we refer the reader to the Appendix.

The expectation values of the frequency and susceptibility matrices contain various combinations of phase factors $\phi_{m\mathbf{q}}$ which describe the coupling of a single CuO_4 plaquette to the surrounding lattice. In most cases the latter can be treated only approximately. However, their omission would lead us back to the diagonalization of a single CuO_4 plaquette and therefore is not justified. There are qualitative differences between the lattice and the plaquette problems: On a CuO_4 plaquette, the operators A_p for doubly occupied oxygen sites can replace the charge-transfer operator A_t , while in the lattice case, there is no singlet binding energy for $U_d \rightarrow \infty$ if the charge-transfer operator is ignored.

If one compares the present set of relevant operators with the one for the photoemission spectra in Ref. 37 the additional inclusion of the charge-density operator A_c is noticed. In the previous calculation a Néel-ordered ground state had been assumed. Starting from that spin order, an operator such as $p_{\uparrow}^\dagger n_{\downarrow}$ is either equal to p_{\uparrow}^\dagger or vanishes completely. Consequently, the charge-density operator can be replaced by the bare creators of oxygen holes in that case.

Similar operators have been used earlier by Fedro and Sinha⁵³ in their approach to the excitation spectrum of the Anderson lattice model in the limit of infinite

Coulomb repulsion U . Besides the operators $p_{\mathbf{k}\uparrow}^\dagger$ and $d_{\mathbf{k}\uparrow}^\dagger - \bar{d}_{\mathbf{k}\uparrow}^\dagger$ the authors included also A_s and A_c , for which they solved the equations of motion. The excitation spectrum of the Emery model for $U_d \rightarrow \infty$ has been calculated by Matsumoto *et al.*²⁹ using a self-consistent equation of motion method. They also took the spin-flip and charge-density operators A_s and A_c into account but in linear combination with other operators. Their results are in agreement with our findings in the infinite U_d limit.

V. COMPARISON WITH EXACT DIAGONALIZATIONS

Having described the self-consistent projection technique, we now present the calculated spectral densities for various different cases. In order to demonstrate the proper choice of the relevant space \mathcal{R} and the validity of the approximations made, we first compare the calculated excitation spectra for small clusters with exact results. Figures 3 and 4 show the spectral functions of an oxygen and a copper hole, respectively, in a 2×2 CuO_2 cluster with periodic boundary conditions at half filling

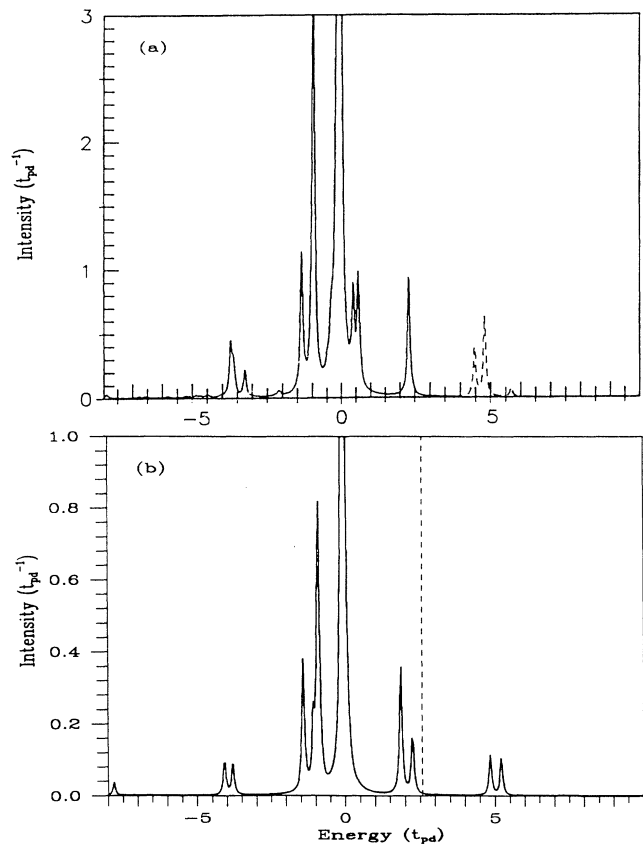


FIG. 3. Oxygen spectrum: (a) presents the exact photoemission (full line) and inverse photoemission spectrum (dashed line) for an oxygen hole in a 2×2 CuO_2 cluster with periodic boundary conditions [Horsch and Stephan (Ref. 54)]. In (b) the self-consistent oxygen spectrum is shown integrated over the k points of a 2×2 cluster. The Fermi energy (dashed line) lies in the energy gap at half filling. Parameter values: $U_d = 6$, $U_p = 3$, $t_{pp} = 0$, $t_{pd} = 1$, $\Delta = 4$, and $n_h = 1$.

($n_h = 1.0$). The upper curves are the exact results as computed by Horsch and Stephan⁵⁴ for the parameter values $U_d = 6$, $U_p = 3$, $\Delta = 4$, $t_{pd} = 1$, and $t_{pp} = 0$. If not stated otherwise, t_{pd} is taken as the unit of energy. Full lines show the photoemission and dashed lines the inverse photoemission spectra. In the lower figures the self-consistent spectral functions for the same parameter set are presented. The intensities are given for one spin direction and only one oxygen orbital. Note, that in the exact results the total copper and oxygen spectral weights are given.

At half filling, the Fermi energy indicated by the dashed lines in Figs. 3 and 4 lies in the energy gap formed by the upper Hubbard band at 5 and the Zhang-Rice singlet states between 0.5 and 2.5. The corresponding triplets appear at -1 and the lower Hubbard band near -4 . The dominating peak in the oxygen spectrum is formed by nonbonding oxygen states. Therefore, this maximum lies at 0, the value of the oxygen on-site energy e_p , and is absent in the copper spectrum. Furthermore, a small oxygen satellite peak is found in the oxygen spectrum at -8 and a structure around -7 in Fig. 4 generated by the charge-transfer operator A_t . All these structures have their counterparts in the exact spectra. They are positioned nearly at the same energies and have similar intensities.

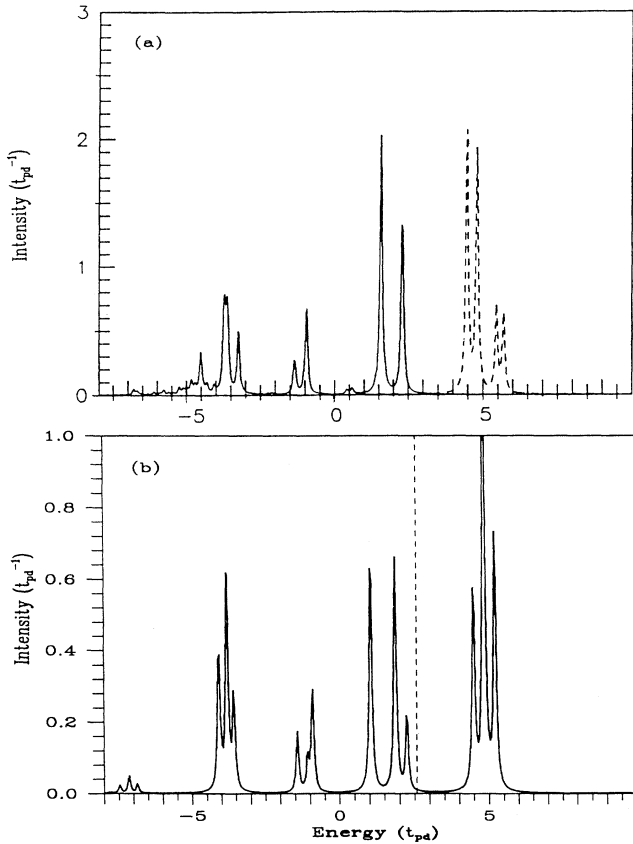


FIG. 4. Copper spectrum: Exact (a) and self-consistent (b) copper spectrum of a 2×2 CuO_2 cluster. Same parameters as in Fig. 3.

A 2×2 cluster with periodic boundary conditions has only three nonequivalent k points, i.e., $(0,0)$, $(\pi,0)$, and (π,π) , which describe the dispersion of the singlet band as well as the upper Hubbard band. In the present approach the excitation energy of the singlet state at half filling is highest at (π,π) and lowest at $(0,0)$ (see also Figs. 9 and 10). This is in contrast to the results of diagonalizations of a 2×2 CuO_2 cluster, where it is found that the excitation energy is highest at $(\pi,0)$ and lowest at (π,π) in the case of half filling. The origin of this discrepancy is an inadequate treatment of the strong short-range antiferromagnetic correlations in the present approach as well as finite-size effects in the diagonalization studies. For symmetry reasons the singlet pole has no weight at $(0,0)$ in the oxygen spectra. Similar statements hold for the upper Hubbard band.

In Fig. 5 the spectral densities of oxygen (full line) and copper (dashed line) are shown for the same parameter values as in Figs. 3 and 4 but integrated over 1600 k points. The different bands discussed before now form smooth structures in the excitation spectrum.

A second test of the accuracy of the present approach is to apply it to the plaquette problem, i.e., to a system where four oxygen orbitals surround a central copper site. As the operator set \mathcal{R} in Sec. IV comprises all relevant hole configurations on a CuO_4 plaquette the calculated spectrum is expected to deviate only slightly from the exact solution. In Table I we compare the positions of the triplet, singlet, and upper Hubbard peak for the half-filled ground state ($n_h = 1$) with exact results. For each case the left-hand column shows the self-consistent value and the right-hand column the exact one. The charge-transfer energy Δ is varied from 1 to 5, while the other parameter values are kept fixed, i.e., $U_d = 8$, $U_p = 0$, $t_{pp} = 0$, and $t_{pd} = 1$. The corresponding spectral weights of the peaks are listed in Table II. They refer to a symmetric oxygen hole with up spin. Obviously, the present approach reproduces the exact values quite accurately. The largest deviations appear for $\Delta = 1$, where the energy difference in the singlet positions amounts to 0.06 and the difference in spectral weight for the upper Hub-

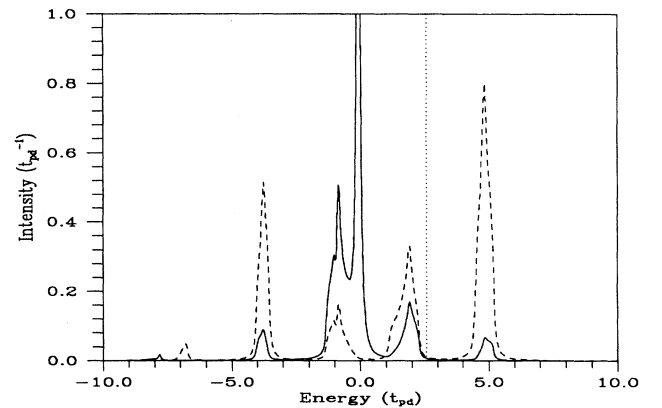


FIG. 5. Copper (dashed line) and oxygen spectrum (full line) integrated over 1600 k points. Same parameters as in Fig. 3.

TABLE I. Positions of the triplet, singlet, and upper Hubbard peaks for the CuO_4 plaquette at half filling: For each peak the self-consistent values are listed in the left-hand column, the exact results in the right-hand one. Parameters are $U_d=8$, $U_p=0$, $t_{pp}=0$, $t_{pd}=1$, and Δ is varied from 1 to 5. Energies are given in units of t_{pd} .

Δ	Triplet		Singlet		Hubbard	
1	-1.565	-1.561	1.253	1.313	2.541	2.561
3	-1.005	-1.000	1.497	1.515	3.996	4.000
5	-0.703	-0.701	1.809	1.813	5.701	5.701

bard peak to 0.013. As has been mentioned before, the operators $A_{\bar{p}}$ and A_t act similarly on a CuO_4 plaquette and therefore only one of them has to be taken into account. The data in Tables I and II have been calculated by including the operators A_p , A_d , $A_{\bar{d}}$, A_s , A_c , and A_t in the relevant set.

The comparison of the self-consistent excitation spectrum with exact results for a single CuO_4 plaquette or a 2×2 CuO_2 cluster illustrates the completeness of the relevant set \mathcal{R} and the accuracy of the approximations for static expectation values. In the next section the composition of the excitations and their dispersion relations will be discussed in detail. The influence of hole doping on the spectral weights of the singlet and upper Hubbard band and on the volume of the Fermi surface are treated in Sec. VII and VIII, respectively.

VI. ANALYSIS OF THE EXCITATION SPECTRUM

In Fig. 6 the excitation spectra of copper (dashed lines) and oxygen holes (full lines) are shown for the parameter values $U_d=8$, $U_p=3$, $t_{pp}=0.5$, $t_{pd}=1$, and $\Delta=4$. At half filling [$n_h=1$, Fig. 6(a)], the Fermi energy lies in the energy gap near the lower edge of the upper Hubbard band at 4.4. As in the preceding figures the singlet band around 2 forms a separate structure, whereas the triplet states near -0.5 merge into the continuum of pure oxygen states because of the direct oxygen-oxygen hopping. In comparison with Ref. 2 we used a slightly higher charge-transfer energy $\Delta=4$, which leads to an energy gap of 1.5 in accordance with experimental values for cuprate superconductors. When the system is doped with additional holes the Fermi energy moves into the singlet band as can be seen in Fig. 6(b), where the hole concentration equals 1.25. The upper Hubbard band appears

TABLE II. Spectral weight of the triplet, singlet, and upper Hubbard peaks for a CuO_4 plaquette at half filling: Same parameters and notation as in Table I.

Δ	Triplet		Singlet		Hubbard	
1	0.459	0.466	0.304	0.314	0.202	0.189
3	0.599	0.600	0.266	0.264	0.101	0.100
5	0.661	0.668	0.224	0.223	0.055	0.055

at higher energies, and its spectral weight has decreased. The missing weight has been shifted to the singlet states near the Fermi energy, which are occupied by holes. We find their total intensity to be given by 0.40 instead of 0.25 the value consistent with the doping concentration.

In order to get more insight into the composition of the different quasiparticle peaks in Fig. 6 one can compare the copper and oxygen spectra with the corresponding spectral functions of the other operators in the relevant set \mathcal{R} . This is done in Fig. 7 for the half-filled case. Besides the usual spectra for oxygen and copper holes (labeled p and d , respectively) also the intensity distribution of the corresponding operators for double occupation (labeled \bar{p} and \bar{d} , respectively) are shown. By considering these curves one may identify the small structure near -8 as an oxygen satellite and the more pronounced peak at -7 as the lower Hubbard band. Furthermore, spectral functions are presented for the singlet and triplet operators, $2^{-\frac{1}{2}}(A_c-A_s)$ (labeled S) and $2^{-\frac{1}{2}}(A_c+A_s)$ (labeled T), respectively. The triplet correlation function has a single maximum at -0.5 . As expected, the largest weight of the singlet operator is concentrated above the triplets near 2. Moreover, the singlet spectrum shows structures close to -4 and -7 , which are due to hybridization with

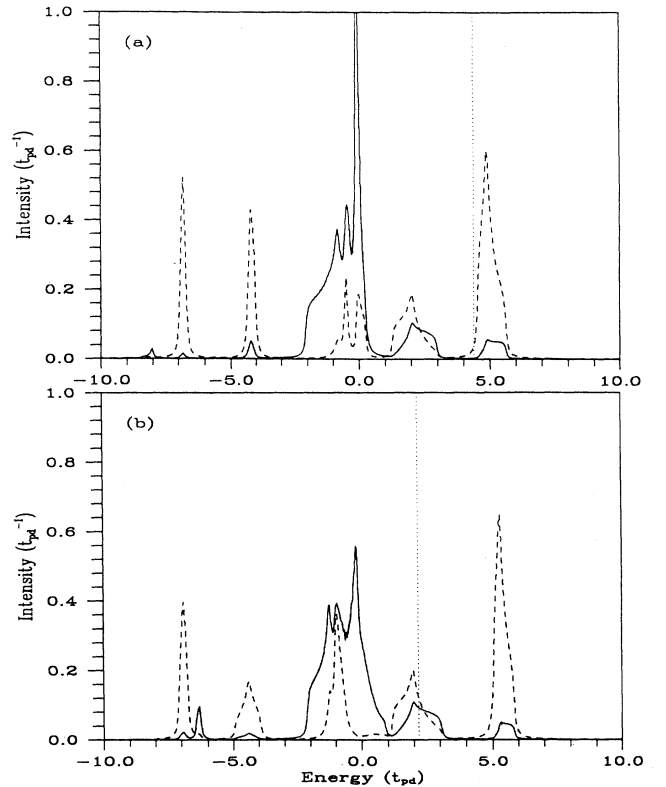


FIG. 6. Copper (dashed lines) and oxygen spectra (full lines) for the parameter set $U_d=8$, $U_p=3$, $t_{pp}=0.5$, $t_{pd}=1$, and $\Delta=4$. Figure (a) presents the spectra at half filling ($n_h=1$), figure (b) for a hole concentration $n_h=1.25$. Upon doping, the Fermi energy (dotted lines) moves from the energy gap in (a) into the singlet band in (b).

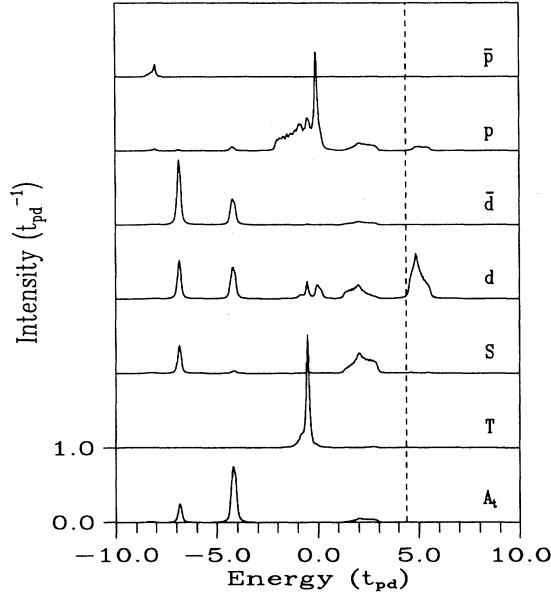


FIG. 7. Spectral functions of relevant operators at half filling (same parameters as in Fig. 6): The curves show from top to bottom the spectral density for the operator creating doubly occupied oxygen sites (labeled \bar{p}), the oxygen spectrum of Fig. 6(a) (labeled p), the spectral distribution of the operator $\bar{d}_{I\uparrow}^\dagger$ (labeled \bar{d}), the copper spectrum of Fig. 6(a) (labeled d), and finally the spectral densities of the operators $2^{-\frac{1}{2}}(A_c - A_s)$ (labeled S), $2^{-\frac{1}{2}}(A_c + A_s)$ (labeled T) as well as A_t (labeled A_t). The dashed line marks the position of the Fermi energy.

other two-hole singlets on a CuO_4 plaquette, i. e., $d_{\uparrow}^\dagger d_{\downarrow}^\dagger| \rangle$ and $p_{\uparrow}^\dagger p_{\downarrow}^\dagger| \rangle$. Indeed the maximum near -4 is dominated by the charge-transfer operator A_t , which creates locally the configuration $p^4 d^{10}$. This can be seen in the lowest curve.

In the present calculation the actual form of the ground state is not determined. Instead ground-state expectation values are calculated self-consistently. Therefore, we must ensure that $2^{-\frac{1}{2}}(A_c - A_s)$ indeed creates a singlet state of the Zhang-Rice type. For that purpose we consider the singlet and triplet correlation functions $C_s = \langle s^\dagger s \rangle$ and $C_t = \langle t^\dagger t \rangle$, where $s^\dagger = 2^{-\frac{1}{2}}(p_{\uparrow}^\dagger d_{\downarrow}^\dagger - p_{\downarrow}^\dagger d_{\uparrow}^\dagger)$ and $t^\dagger = 2^{-\frac{1}{2}}(p_{\uparrow}^\dagger d_{\uparrow}^\dagger + p_{\downarrow}^\dagger d_{\downarrow}^\dagger)$ as before. The singlet (triplet) expectation value C_s (C_t) can be determined self-consistently from the relation

$$C_{s(t)} = \frac{1}{N} \sum_{\mathbf{q}} \langle [A_c(\mathbf{q}) \mp A_s(\mathbf{q})] p_{\mathbf{q}\uparrow} \rangle, \quad (28)$$

where the minus sign refers to C_s . The doping dependence of these expectation values is illustrated in Fig. 8. At half filling, the singlet as well as the triplet weight in the ground-state wave function are very low. Upon doping the Fermi energy moves as seen in Fig. 6. Simultaneously the singlet weight increases rapidly, roughly proportional to the hole concentration. In contrast to that the triplet weight in the ground-state remains small. Thus we may conclude that the states around 2 in Fig. 6

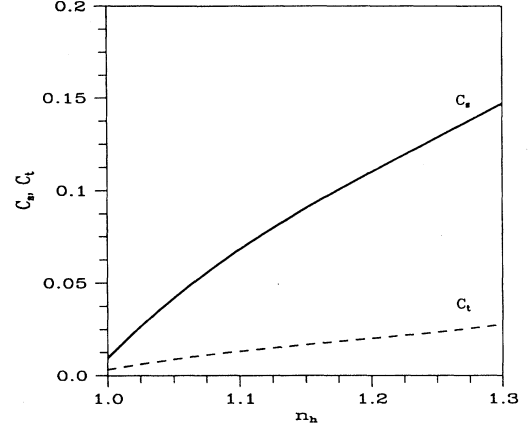


FIG. 8. The static expectation values of the singlet and triplet operators C_s and C_t , respectively, as a function of hole concentration n_h . Same parameters are in Fig. 6.

are of the Zhang-Rice singlet type.

Next the dispersion relations of the nine poles at half filling are shown in Fig. 9. The parameters are the same as in Fig. 6. For the singlet band around 2 and the upper Hubbard band at 5 a free-particle-like dispersion is found originating from nearest-neighbor hopping. Compared to tight-binding or Hartree-Fock solutions for the Emery model the bandwidths are strongly reduced, namely, to 1.7 for the singlet band and to 1.1 in case of the upper Hubbard band. The satellite bands beyond -3 are nearly dispersionless.

In Fig. 9 the position of the Fermi energy, or more precisely the position of the chemical potential is in the energy gap. In order to obtain good convergence for a finite set of k points, all calculations have been done at finite temperatures. In case of hole concentrations $n_h > 1$ a temperature of $kT = 10^{-3}$ has been used. At half filling, the spectra have been computed for $kT = 0.1$. Only in that case is the chemical potential exactly situated in the gap. If the temperature is lowered to $kT = 10^{-3}$

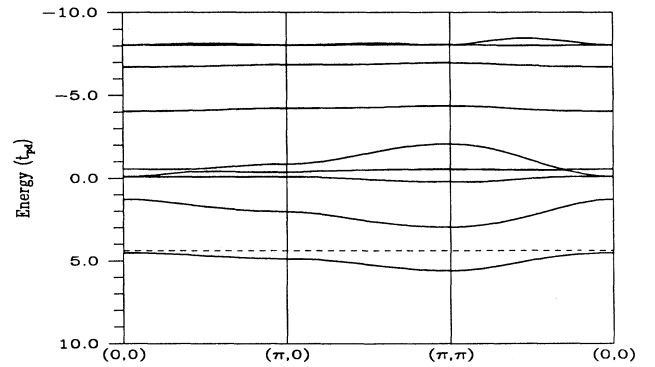


FIG. 9. Dispersion of the nine relevant poles along high symmetry directions in the Brillouin zone at half filling. Parameters are the same as in Fig. 6. The dashed line denotes the Fermi energy.

the chemical potential is positioned in the upper Hubbard band due to the approximations used. However, the deviation of the Fermi volume of holes from the total volume of the Brillouin zone is in the range of 1%. On the other hand one can determine self-consistently the hole concentration n_h at $kT = 10^{-3}$, for which the Fermi energy lies in the gap. One finds $n_h = 1.005$. These slight differences are considered to be an artifact of the approximations for the static expectation values in the frequency and susceptibility matrices.

The present calculation starting from a paramagnetic ground state shows explicitly that the energy gap and the insulating behavior of the half-filled Emery model is not caused by antiferromagnetic order but through the formation of highly correlated Zhang-Rice singlet states. Consequently, the energy gap separating the singlet states from the upper Hubbard band is also present when the long-range antiferromagnetic order is destroyed due to hole doping. This result is in agreement with exact diagonalization studies of small clusters.

Shown in Fig. 10 is the singlet band (full line) for the parameter values $U_d = 6$, $\Delta = 4$ at a hole concentration of $n_h = 1.25$. The figure contains also the quantum Monte Carlo (QMC) data (open squares) and exact diagonalization results (solid squares) calculated by Dopf *et al.*²⁰ The Fermi levels of the QMC calculation (4×4 CuO₂ cluster) and of the exact diagonalization (2×2 CuO₂ cluster) have been shifted to coincide with the present one. As can be seen the three curves are in quantitative agreement and show the form of dispersion observed in experiments for high-temperature superconductors (HTSC).³⁸⁻⁴¹ The bandwidth $W_s = 1.37$ obtained by the projection technique exceeds the diagonalization value of $W_s = 1.21$ and the QMC result of $W_s = 1.0$. However, the experimental width of the band crossing the Fermi level in a HTSC such as Bi₂Sr₂CaCu₂O₈ for a hole concentration of 20% is somewhat smaller. The part of the band observed in photoemission appears in a

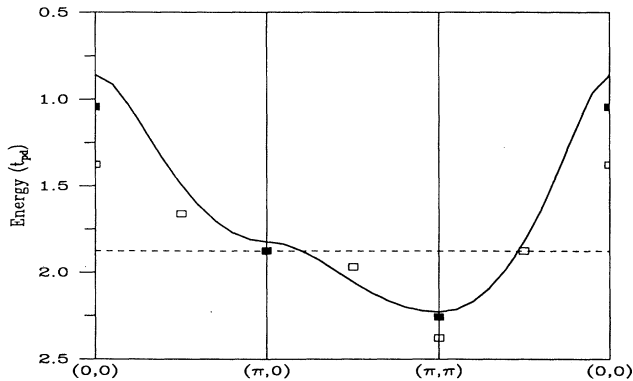


FIG. 10. Dispersion of the singlet pole (full line) for the parameter values $U_d = 6$, $U_p = 0$, $t_{pp} = 0$, $t_{pd} = 1$, $\Delta = 4$ and a hole concentration of $n_h = 1.25$. The open squares present quantum Monte Carlo data for a 4×4 CuO₂ cluster at an inverse temperature of $\beta = 10$. The solid squares are exact diagonalization results for a 2×2 CuO₂ cluster [Dopf *et al.* (Ref. 20)].

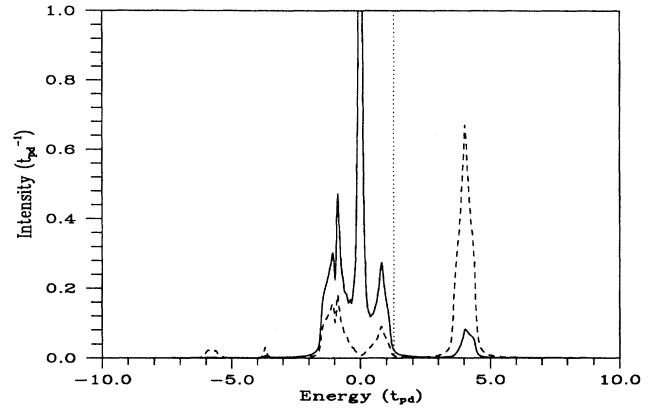


FIG. 11. Copper (dashed line) and oxygen spectral functions (full line) for the parameter values $U_d = 100$, $U_p = 0$, $t_{pp} = 0$, $t_{pd} = 1$, $\Delta = 3$ at half filling. The Fermi energy is denoted by the dotted line.

range of 0.25 eV below the Fermi energy. In IPES the unoccupied states close to the Fermi level are detected in a maximal distance of 0.65 eV.⁴¹

Finally, we compare spectra calculated here for a paramagnetic ground-state with the previous ones,³⁷ where an antiferromagnetic ground state and $U_d \rightarrow \infty$ had been assumed. Figure 11 shows the spectral functions in the large U_d limit ($U_d = 100$, $\Delta = 3$) at half filling, which should be compared with Fig. 4 in Ref. 37. Qualitatively, the antiferromagnetic order does not change the k -integrated spectra very much. In both cases the singlet and triplet peaks appear at similar excitation energies near ± 1 . On the other hand, the singlet dispersion is completely different. The singlet band in Ref. 37 shows antiferromagnetic symmetry, i.e., the k points $(0, 0)$ and (π, π) are degenerate and lowest in energy. Furthermore, the width of the singlet band $W_s = 0.2$ is very small. This suggests that taking into account short-range antiferromagnetic correlations in the self-consistent approach will reduce the singlet bandwidth to the experimental value.

VII. SHIFT OF SPECTRAL WEIGHT

The influence of doping on the low-lying excited states in cuprate superconductors is of crucial importance for understanding their properties. We therefore study in more detail the influence of additional holes on the singlet states and the upper Hubbard band. For low values of the charge-transfer energy Δ the changes are quite pronounced as illustrated in Fig. 12. The dashed line shows the singlet and upper Hubbard band in the copper spectrum for $\Delta = 2$, $U_d = 6$ at half filling, where the full line is for $n_h = 1.25$. Obviously, the upper Hubbard band loses, upon hole doping, a considerable part of its intensity while being shifted to higher energies. This spectral weight is transferred to the singlet states, which roughly keep their positions. Simultaneously the width of the free-particle-like singlet band increases.

The amount of spectral weight transferred to the singlet states depends upon the size of t_{pd} . We measure

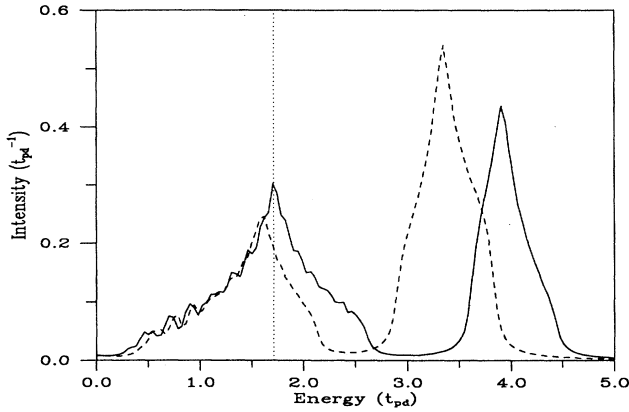


FIG. 12. Transfer of spectral weight caused by hole doping: The copper spectrum is shown at half filling (dashed line) and for a hole concentration of $n_h = 1.25$ (full line). Parameters are $U_d = 6$, $U_p = 0$, $t_{pp} = 0$, $t_{pd} = 1$ and $\Delta = 2$. The dotted line marks the position of the Fermi energy for $n_h = 1.25$.

the weight of occupied singlet states I_{sing} by integrating the total spectral intensity of copper and oxygen holes from the middle of the energy gap up to the Fermi level. In Fig. 13 the full lines show I_{sing} as a function of hole concentration n_h for four different values of t_{pd} . The remaining parameters $U_d = 8$, $U_p = 0$, $2t_{pp} = 0.25$, and $\Delta = 4$ are kept fixed. Without copper-oxygen hopping ($t_{pd} = 0$), I_{sing} equals the concentration of added holes and grows as in a normal semiconductor like the dashed curve. When $\sqrt{2}t_{pd}$ is increased from 0.5 (bottom curve) to 2 in steps of 0.5, more and more spectral weight is transferred from the upper Hubbard band to the states near the Fermi energy and the curves become steeper. At a hole concentration of $n_h = 1.25$ our data can be compared with exact

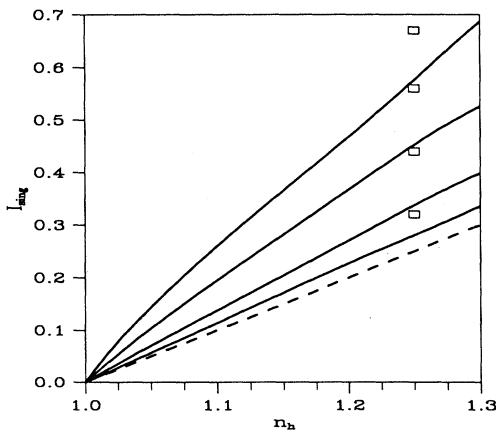


FIG. 13. Singlet weight I_{sing} as a function of hole concentration n_h : The copper-oxygen hopping t_{pd} is increased from $\sqrt{2}t_{pd} = 0.5$ (lowest curve) to $\sqrt{2}t_{pd} = 2$ (highest curve) in steps of 0.5, while the other parameters $U_d = 8$, $U_p = 0$, $2t_{pp} = 0.25$, and $\Delta = 4$ are kept fixed. Open squares present exact data for a 2×2 CuO_2 cluster (Ref. 13). The dashed curve corresponds to the case $t_{pd} = 0$.

diagonalization results of Eskes *et al.*¹³ and reasonable agreement is found.

The spectral weights of poles forming the singlet and upper Hubbard band possess a pronounced k dependence, which is presented in Fig. 14 along high symmetry directions. In part (a) the total spectral weights (full lines) of the singlet poles are shown as well as the copper (dashed) and oxygen (dotted) contributions. The same notation is used for the upper Hubbard band in Fig. 14(b). In both figures, the thick lines correspond to a hole concentration of $n_h = 1.25$, whereas the thin lines refer to the half-filled case. Parameters are the same as in Fig. 6.

Consider first the total weights of poles in the upper Hubbard band at half filling. In a system of independent particles each k point can be occupied by two electrons with opposite spin directions. Therefore, the total spectral weight equals 2 over the whole Brillouin zone. In distinction, the mean value of the pole strengths for the upper Hubbard band gives 1 leading to an insulator at half filling. Moreover, the pole strengths are low around $(0,0)$ and show a maximum at (π, π) . This is mainly a consequence of the oxygen contribution to the total spectral weight, which vanishes at $(0,0)$. For symmetry reasons there is no symmetric linear combination at this k

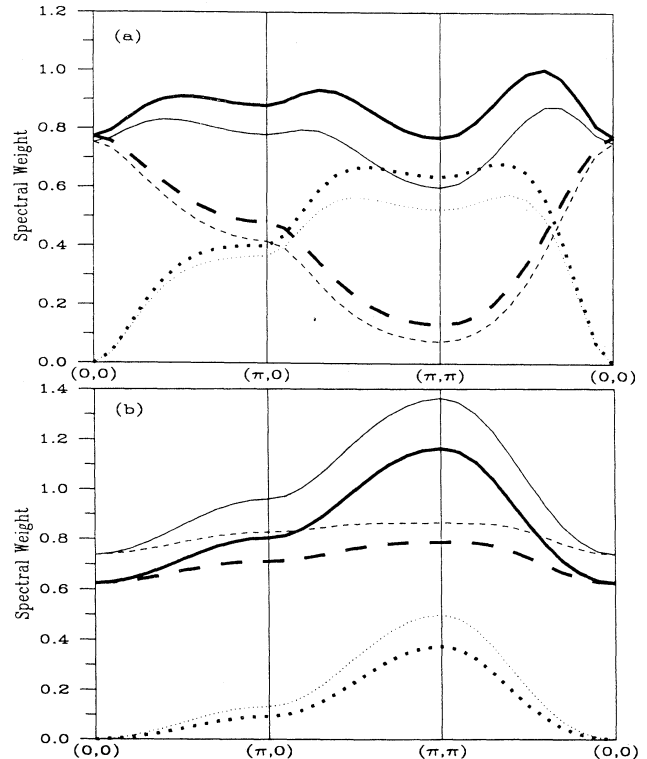


FIG. 14. Spectral weight of the singlet (a) and upper Hubbard poles (b) along high-symmetry directions in the Brillouin zone: Part (a) shows the total singlet pole strength (full lines), the copper (dashed) and the oxygen (dotted) contribution both for $n_h = 1.0$ (thin) and $n_h = 1.25$ (thick). The same notation is used for the upper Hubbard poles in (b). Same parameters as in Fig. 6.

point, which implies vanishing hybridization between the copper and oxygen system. When the system is doped with 25% holes the total pole strengths decrease roughly about 15% at all k points. The decrease affects the copper as well as the oxygen contribution. Around (π, π) the change is maximal. As discussed before, this spectral weight is transferred to the singlet states.

The pole strengths in the singlet band at half filling lie around 0.8. They are lowest at (π, π) and reach their maximum value in the middle of the diagonal between (π, π) and (σ, σ) . As for the upper Hubbard band the oxygen spectral weight vanishes at $(0, 0)$ for the same reasons. Remarkable is the high oxygen contribution to states near (π, π) , since precisely these states are occupied by holes at a doping concentration of 25%. Therefore, the oxygen share of occupied singlets is about 75%, whereas the total singlet band consists only to 50% out of oxygen for the parameter values of Fig. 6. Upon doping the residues of the singlet poles increase. The effect is most pronounced at (π, π) . Consequently, the rise in spectral weight of the singlet band counteracts the corresponding loss in the upper Hubbard band. Note, that an increase in pole strength occurs for all k points, in particular also for the unoccupied ones. It follows, that there is also a transfer of weight to states near the Fermi energy in the photoemission spectrum.

Van Veenendaal *et al.*⁵⁵ investigated the doping dependence of the Fermi level in $\text{Bi}_2\text{Sr}_2\text{Ca}_{1-x}\text{Y}_x\text{Cu}_2\text{O}_{8+\delta}$ by studying its core-level spectrum in the range of $0 \leq x \leq 1$. Upon hole doping, i.e., by decreasing x from $x = 1.0$, where the compound is an insulator, to $x = 0$, the Fermi energy moves into the valence band. The position of the Fermi level as a function of doping was found to be consistent with a rectangular density of states of width 1 eV and one hole per state. These findings qualitatively agree with the singlet bandwidth of Fig. 10 and the spectral weight of the singlet poles in Fig. 14(a).

VIII. FERMI SURFACE

After discussing the influence of doping on the spectral weight of the singlet band we finally turn to the problem of the Fermi surface. As it is well known a compound such as $\text{La}_{2-x}\text{Sr}_x\text{CuO}_4$ is a semiconductor for $x = 0$. Upon doping one expects that the number of charge carriers equals the number of added holes. Several measurements of transport quantities such as electrical conductivity, Hall coefficient, etc., support this point of view. The Hall carrier density in $\text{La}_{2-x}\text{Sr}_x\text{CuO}_4$, for example, increases proportional to the doping concentration.^{56,57} Moreover, the infrared conductivity of La_2CuO_4 shows a gap below 2 eV. Upon doping the Drude weight increases proportional to the number of added holes.^{58,59} Consequently, also the volume of the Fermi sphere should correspond to the number of added holes. On the other hand, ARPES experiments^{45,46} on $\text{Bi}_2\text{Sr}_2\text{CaCu}_2\text{O}_8$ clearly reveal a large Fermi surface enclosing a volume consistent in size with the total number of valence electrons in the system. This result is in agreement with Luttinger's theorem⁴⁸ stating that the Fermi volume of a noninteracting electron system is not affected by many-particle in-

teractions. Consequently, it can be derived directly from the number of electrons per unit cell.

The proof of Luttinger's theorem is based on the analyticity of the electronic Green's function with respect to the interaction strength. Therefore, the theorem does not apply necessarily to a strongly correlated system. Here, we have started from a small cluster including the strong correlations right from the beginning and considered the hybridization with the other clusters in the lattice as the perturbation.

Figure 15 illustrates the Fermi surface for the parameters of Fig. 6 and a hole concentration of $n_h = 1.25$. It follows as a byproduct from the previous calculations. The open circles denote k points occupied by holes in the Brillouin zone. Although there is no Fermi surface at half filling for 25% doping is rather large. The ratio between the Fermi volume of holes V_F and the volume of the first Brillouin zone V_{BZ} is found to be 0.44 instead of 0.125 corresponding to a small surface. However, the value is smaller than 0.625 as required by Luttinger's theorem. When the doping concentration is further increased, the difference between the self-consistent result and the Fermi volume of independent particles becomes smaller and smaller. Consequently, there is a tendency to restore the large Fermi sphere upon doping.

This point is further illustrated by Fig. 16. It shows the ratio between V_F and V_{BZ} as a function of hole concentration n_h for three different values of the charge-transfer energy Δ , while the remaining parameters $U_d = 6$, $U_p = 0$, $t_{pp} = 0$, and $t_{pd} = 1$ are kept fixed. The dashed line represents the curve for the large sphere, the dotted refers to the small one. For $\Delta = 2$ (full line on top) the self-consistent Fermi volume reaches Luttinger's result at $n_h = 1.4$. If Δ is increased to 3, 4, where we find insulators at half filling, the volume rises slower but shows the same tendency. Therefore, one may state that for $n_h = 1.25$ and $\Delta = 3$ a Fermi surface is obtained, which lies already close to the large one.

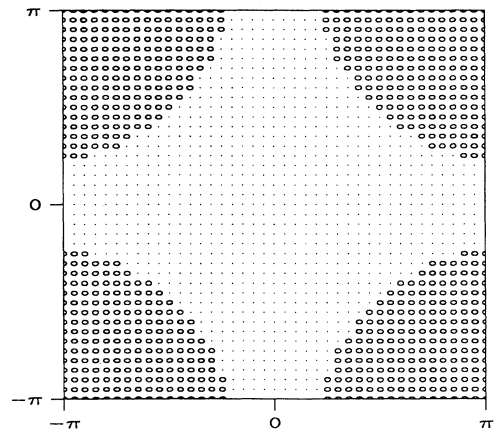


FIG. 15. Fermi surface for a hole concentration of $n_h = 1.25$ and parameters as in Fig. 6: Open circles denote k points occupied by holes.

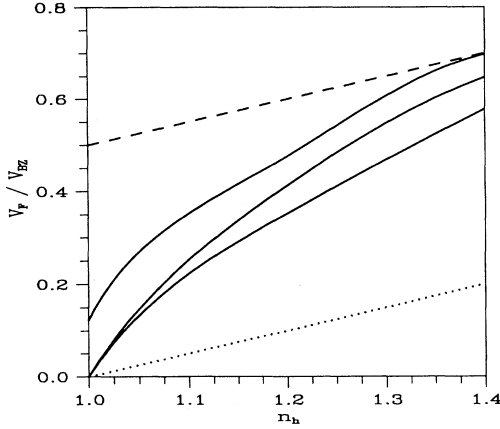


FIG. 16. Volume of the Fermi sphere as a function of hole concentration n_h : The charge-transfer energy is increased from $\Delta = 2$ (highest full line) to $\Delta = 4$ (lowest full line) in steps of 1, while the parameters $U_d = 6$, $U_p = 0$, $t_{pp} = 0$, and $t_{pd} = 1$ are kept fixed. The volume of the large (small) Fermi surface is illustrated by the dashed (dotted) line.

IX. CONCLUSION

It has been demonstrated that the excitation spectrum of the Emery model can be computed accurately by solving self-consistently the projection equations (9) of the relevant operator set \mathcal{R} . Within that approach the parameters for the Coulomb repulsion U_d , the oxygen-oxygen hopping t_{pp} or the charge-transfer energy Δ can be freely varied.

The system exhibits an energy gap between the singlet states of the Zhang-Rice type and the upper Hubbard band. At parameter values realistic for the cuprate materials an insulator is formed in case of half filling. Upon hole doping the Fermi energy moves into the singlet band, which leads to an increase in spectral weight of all singlet states. For a doping concentration of 20% the free-particle-like dispersion of the singlet band agrees

with ARPES experiments on $\text{Bi}_2\text{Sr}_2\text{CaCu}_2\text{O}_8$, although the measured width of the band crossing the Fermi level is smaller by a factor of order 2. At this hole concentration the calculated Fermi surface lies close to the experimental data, which reveal a large volume consistent in size with Luttinger's theorem.

The good agreement of the present results with exact diagonalizations of small clusters and quantum Monte Carlo studies suggests that the approximations for the static expectation values of the frequency and susceptibility matrix are well justified. Furthermore, the cluster calculations support our choice of relevant operators. They form the minimal basis for the description of single-particle excitations in the Emery model.

ACKNOWLEDGMENTS

We would like to thank H. Eskes, P. Horsch, Y. Ohta, and T. Tohyama for helpful remarks concerning the interpretation of exact diagonalization studies.

APPENDIX: FREQUENCY AND SUSCEPTIBILITY MATRICES

The frequency and susceptibility matrix elements, which will be given in the following, are functions of local occupation numbers n_{xy} :

$$n_{xy} = \frac{1}{N} \sum_{\mathbf{q}} \langle A_x(\mathbf{q}) A_y^\dagger(\mathbf{q}) \rangle.$$

The indices x and y are elements of the set $\{p, d, \bar{d}, s, c, t, d', \bar{p}\}$ replacing the corresponding operators $p_{\mathbf{q}\uparrow}^\dagger$, $d_{\mathbf{q}\uparrow}^\dagger$, $\bar{d}_{\mathbf{q}\uparrow}^\dagger$, $A_s(\mathbf{q})$, $A_c(\mathbf{q})$, $A_t(\mathbf{q})$ and $d_{\mathbf{q}\uparrow}^\dagger = \sum_m |\phi_{m\mathbf{q}}|^2 d_{\mathbf{q}\uparrow}^\dagger$, as well as $\bar{p}_{\mathbf{q}\uparrow}^\dagger = \sum_m \phi_{m\mathbf{q}} \bar{c}_{m\mathbf{q}\uparrow}^\dagger$, respectively. As mentioned in Sec. III, expectation values of the form $\langle A_x(\mathbf{q}) A_y^\dagger(\mathbf{q}) \rangle$ can be determined self-consistently from the corresponding spectral function $S_{yx}(\mathbf{q}, \omega)$ using Eq. (13). In addition, we introduce here the following abbreviations:

$$n_p = \frac{1}{N} \sum_{\mathbf{q}} n_{mm}(\mathbf{q}), \quad n_d = \frac{1}{N} \sum_{\mathbf{q}} n_{dd}(\mathbf{q}),$$

$$n_{pd}^\epsilon = \frac{1}{N} \sum_{m\mathbf{q}} \epsilon_{m\mathbf{q}} \phi_{m\mathbf{q}} n_{md}(\mathbf{q}), \quad n_{pp}^\epsilon = \frac{1}{N} \sum_{m\mathbf{q}} \epsilon_{m\mathbf{q}} \phi_{m\mathbf{q}} \phi_{n\mathbf{q}}^* n_{mn}(\mathbf{q}),$$

$$W_{p\bar{d}} = n_{p\bar{d}} + n_{\bar{d}p} - n_{pd}, \quad W_{d\bar{p}} = n_{d\bar{p}} + n_{\bar{p}d} - n_{pd},$$

$$W_{pp} = \frac{1}{N} \sum_{m\mathbf{q}} \epsilon_{m\mathbf{q}} \{n_{m\bar{m}}(\mathbf{q}) + n_{\bar{m}m}(\mathbf{q}) - n_{mm}(\mathbf{q})\}.$$

Thereby, the index $m = 1, 2$ refers to an oxygen creation operator $c_{m\mathbf{q}\uparrow}^\dagger$, and \bar{m} replaces $\bar{c}_{m\mathbf{q}\uparrow}^\dagger$. According to this convention the static but \mathbf{q} -dependent expectation value $n_{m\bar{m}}(\mathbf{q})$, for example, stands for $n_{m\bar{m}}(\mathbf{q}) = \langle c_{m\mathbf{q}\uparrow}^\dagger \bar{c}_{m\mathbf{q}\uparrow} \rangle$. The constants n_p and n_d are the local occupation numbers of oxygen and copper sites, respectively, for one spin direction. Finally it is convenient to define the two functions $\alpha_{\mathbf{k}} = \sum_m |\phi_{m\mathbf{k}}|^2$ and $\beta_{\mathbf{k}} = \sum_m |\phi_{m\mathbf{k}}|^2 \epsilon_{m\mathbf{k}}$.

1. Susceptibility matrix

After the introduction of the notation for the occupation numbers we proceed with the equations for susceptibility matrix elements: $X_{xy}(\mathbf{k}) = (A_x^\dagger(\mathbf{k}) | A_y(\mathbf{k}))$. As before, the letters d, s, c , and t stand for the operators $d_{\mathbf{k}\uparrow}^\dagger$, $A_s(\mathbf{k})$, $A_c(\mathbf{k})$, and $A_t(\mathbf{k})$, respectively. In case of oxygen operators $c_{m\mathbf{k}\uparrow}^\dagger$, $\bar{c}_{m\mathbf{k}\uparrow}^\dagger$ (indices p and \bar{p} , respectively) two bands are to be distinguished by the indices $m, n = 1, 2$.

For copper and oxygen operators with singly and doubly occupancy we find the expressions

$$\begin{aligned} X_{pp}(m, n, \mathbf{k}) &= \delta_{mn}, & X_{dd}(\mathbf{k}) &= 1, & X_{dp}(m, \mathbf{k}) &= 0, & X_{pd}(m, \mathbf{k}) &= 0, \\ X_{\bar{p}\bar{p}}(m, n, \mathbf{k}) &= \delta_{mn}n_p, & X_{\bar{d}\bar{d}}(\mathbf{k}) &= n_d, & X_{\bar{p}\bar{d}}(m, \mathbf{k}) &= 0, & X_{\bar{d}\bar{p}}(m, \mathbf{k}) &= 0, \\ X_{p\bar{p}}(m, n, \mathbf{k}) &= \delta_{mn}n_p, & X_{d\bar{d}}(\mathbf{k}) &= n_d, & X_{d\bar{p}}(m, \mathbf{k}) &= 0, & X_{\bar{p}d}(m, \mathbf{k}) &= 0. \end{aligned}$$

The susceptibility matrix elements of the spin-flip operator $A_s(\mathbf{k})$ are of the form

$$X_{sp}(m, \mathbf{k}) = 0, \quad X_{sd}(\mathbf{k}) = -n_{dp}, \quad X_{s\bar{p}}(m, \mathbf{k}) = I_m^2(\mathbf{k}), \quad X_{s\bar{d}}(\mathbf{k}) = -n_{\bar{d}p}, \quad X_{ss}(\mathbf{k}) = n_{cp} + n_d - n_{\bar{d}\bar{d}}.$$

For the charge density operator $A_c(\mathbf{k})$ we obtain the equations

$$\begin{aligned} X_{cp}(m, \mathbf{k}) &= \phi_{m\mathbf{k}}^* n_d, & X_{cd}(\mathbf{k}) &= 0, & X_{c\bar{d}}(\mathbf{k}) &= 0, & X_{cs}(\mathbf{k}) &= n_{sp}, \\ X_{c\bar{p}}(m, \mathbf{k}) &= \phi_{m\mathbf{k}}^* n_p n_d - I_m^2(\mathbf{k}), & X_{cc}(\mathbf{k}) &= \alpha_{\mathbf{k}} n_d^2 + I^3(\mathbf{k}). \end{aligned}$$

The list of matrix elements is completed by the expressions for the transfer operator $A_t(\mathbf{q})$:

$$\begin{aligned} X_{tp}(m, \mathbf{k}) &= \phi_{m\mathbf{k}}^* n_{dp}, & X_{td}(\mathbf{k}) &= 0, & X_{t\bar{d}}(\mathbf{k}) &= n_{dt}, & X_{t\bar{p}}(m, \mathbf{k}) &= \phi_{m\mathbf{k}}^* n_{dp} n_p + I_m^4(\mathbf{k}), \\ X_{ts}(\mathbf{k}) &= -n_{ds} - n_{pt}, & X_{tc}(\mathbf{k}) &= \alpha_{\mathbf{k}} n_d n_{dp} + n_{pt} - I^8(\mathbf{k}), & X_{tt}(\mathbf{k}) &= n_{\bar{p}\bar{p}} - n_{pc} + I^9(\mathbf{k}). \end{aligned}$$

The functions $I_m^1(\mathbf{k}), \dots, I_m^{14}(\mathbf{k})$ represent expressions involving double integrations over the reciprocal space. Their definitions will be given following the list of frequency matrix elements in subsection 3.

2. Frequency matrix

The frequency matrix elements are defined as $F_{xy}(\mathbf{k}) = (A_x^\dagger(\mathbf{k}) | \mathcal{L} A_y(\mathbf{k}))$. We start with the matrix elements for the operators $A_p(m, \mathbf{k})$, $A_d(\mathbf{k})$, $A_{\bar{p}}(m, \mathbf{k})$, and $A_{\bar{d}}(\mathbf{k})$:

$$\begin{aligned} F_{pp}(m, n, \mathbf{k}) &= \delta_{mn}(\epsilon_{m\mathbf{k}} + U_p n_p), & F_{dd}(\mathbf{k}) &= e_d + U_d n_d, & F_{dp}(m, \mathbf{k}) &= 2t_{pd}\phi_{m\mathbf{k}}^*, \\ F_{pd}(m, \mathbf{k}) &= F_{dp}^*(m, \mathbf{k}), & F_{\bar{p}\bar{p}}(m, n, \mathbf{k}) &= \delta_{mn}(\epsilon_{m\mathbf{k}} + U_p) n_p, & F_{\bar{d}\bar{d}}(\mathbf{k}) &= (e_d + U_d) n_d, \\ F_{\bar{d}\bar{p}}(m, \mathbf{k}) &= 2t_{pd}\phi_{m\mathbf{k}}^* n_d, & F_{\bar{d}\bar{d}}(\mathbf{k}) &= (e_d + U_d) n_d + 2t_{pd}W_{p\bar{d}}, & F_{\bar{p}d}(m, \mathbf{k}) &= 2t_{pd}\phi_{m\mathbf{k}} n_p, \\ F_{p\bar{d}}(m, \mathbf{k}) &= F_{\bar{d}\bar{p}}^*(m, \mathbf{k}), & F_{\bar{d}\bar{p}}(m, \mathbf{k}) &= 2t_{pd}\phi_{m\mathbf{k}}^* n_p n_d - 6t_{pd}I_m^2(\mathbf{k}), \\ F_{\bar{p}\bar{p}}(m, n, \mathbf{k}) &= \delta_{mn}[(2e_p + U_p) n_p + \epsilon_{m\mathbf{k}} n_p^2 + \frac{1}{2}(W_{p\bar{p}} + 2t_{pd}W_{d\bar{p}}) - 3I_m^1(\mathbf{k})]. \end{aligned}$$

If the expectation values $W_{p\bar{d}}$, $W_{d\bar{p}}$, $W_{p\bar{p}}$ and the integrals I_m^1 , I_m^2 are neglected in the matrix elements $F_{\bar{p}\bar{p}}$, $F_{p\bar{d}}$, $F_{\bar{d}\bar{p}}$, and $F_{\bar{d}\bar{d}}$ the well-known Hubbard I approximation⁵² for a three-band model is recovered. The corresponding susceptibility matrix of the operators A_p , A_d , $A_{\bar{p}}$, and $A_{\bar{d}}$ is exact and remains unchanged. Inclusion of the terms $W_{p\bar{d}}$, $W_{d\bar{p}}$, and $W_{p\bar{p}}$ in the frequency matrix leads to the so-called POMF (projection operator mean field) approximation, discussed in Ref. 36. Finally the full projection onto the operator space of singly and doubly occupancy creates the additional terms I_m^1 and I_m^2 .

We proceed by listing the frequency matrix elements of the spinflip operator $A_s(\mathbf{k})$:

$$\begin{aligned} F_{sp}(m, \mathbf{k}) &= 2t_{pd}\phi_{m\mathbf{k}}^* X_{sd}(\mathbf{k}) + U_p X_{s\bar{p}}(m, \mathbf{k}), & F_{sd}(\mathbf{k}) &= e_d X_{sd}(\mathbf{k}) + U_d X_{s\bar{d}}(\mathbf{k}), \\ F_{s\bar{p}}(m, \mathbf{k}) &= U_p X_{s\bar{p}}(m, \mathbf{k}) - 2t_{pd}[\phi_{m\mathbf{k}}^* n_p n_{dp} + I_m^4(\mathbf{k})] + I_m^5(\mathbf{k}), \\ F_{s\bar{d}}(\mathbf{k}) &= (e_d + U_d) X_{s\bar{d}}(\mathbf{k}) - 2t_{pd}[X_{ss}(\mathbf{k}) - n_{ps}], \\ F_{ss}(\mathbf{k}) &= U_p n_p X_{ss}(\mathbf{k}) + n_{dp} n_{pd}^\epsilon + 2t_{pd}[n_{tp} + n_{dc} - n_d n_{pd'} - n_{dp}(1 - n_{dd'})] + I^6(\mathbf{k}). \end{aligned}$$

The charge-density operator $A_c(\mathbf{k})$ is connected with the other relevant operators by the following frequency terms:

$$\begin{aligned} F_{cp}(m, \mathbf{k}) &= \epsilon_{m\mathbf{k}} X_{cp}(m, \mathbf{k}) + U_p X_{cp}(m, \mathbf{k}), & F_{c\bar{d}}(\mathbf{k}) &= 2t_{pd}[n_{dt} + X_{cc}(\mathbf{k}) - X_{cs}(\mathbf{k})], \\ F_{cc}(\mathbf{k}) &= U_p n_p X_{cc}(\mathbf{k}) + \beta_{\mathbf{k}} n_d^2 + 2t_{pd}(2n_{pt} - n_{dp}) + I^6(\mathbf{k}), & F_{cd}(\mathbf{k}) &= 2t_{pd}\alpha_{\mathbf{k}} n_d, \\ F_{cs}(\mathbf{k}) &= U_p n_p X_{cs}(\mathbf{k}) - n_{dp}^\epsilon + 2t_{pd}[n_{sd'} - n_{ds} - n_{tp} - \alpha_{\mathbf{k}} n_d n_{pd} + I^8(\mathbf{k})], \\ F_{c\bar{p}}(m, \mathbf{k}) &= \epsilon_{m\mathbf{k}} \phi_{m\mathbf{k}}^* n_p n_d + U_p X_{c\bar{p}}(m, \mathbf{k}) + 2t_{pd}I_m^4(\mathbf{k}) - I_m^5(\mathbf{k}). \end{aligned}$$

Finally, the corresponding expression for the charge-transfer operator $A_t(\mathbf{k})$ are presented:

$$\begin{aligned}
F_{t\bar{p}}(m, \mathbf{k}) &= \epsilon_{m\mathbf{k}} X_{t\bar{p}}(m, \mathbf{k}) + U_p X_{t\bar{p}}(m, \mathbf{k}), & F_{td}(\mathbf{k}) &= 2t_{pd} \sum \phi_{m\mathbf{k}} X_{t\bar{p}}(m, \mathbf{k}) + U_d X_{t\bar{d}}(\mathbf{k}), \\
F_{t\bar{p}}(m, \mathbf{k}) &= \epsilon_{m\mathbf{k}} \phi_{m\mathbf{k}}^* n_p n_{dp} + U_p X_{t\bar{p}}(m, \mathbf{k}) + I_m^{10}(\mathbf{k}) - 2t_{pd} I_m^7(\mathbf{k}), \\
F_{t\bar{d}}(\mathbf{k}) &= (e_d + U_d) X_{t\bar{d}}(\mathbf{k}) + 2t_{pd} (\alpha_{\mathbf{k}} n_d n_{dp} + 2n_{pt} + n_{ds}) - 2t_{pd} I^8(\mathbf{k}), \\
F_{ts}(\mathbf{k}) &= (2n_p U_p - e_d) X_{ts}(\mathbf{k}) - U_d (n_{p\bar{d}} - n_{\bar{p}d}) - n_{pd}^e n_{pp} - n_{pp}^e n_{pd} \\
&\quad + 2t_{pd} (2n_{ps} - n_{cp} + n_{\bar{d}d}) + I^{11}(\mathbf{k}) - 2t_{pd} I^9(\mathbf{k}), \\
F_{tc}(\mathbf{k}) &= (2n_p U_p - e_d) X_{tc}(\mathbf{k}) - U_d n_{\bar{p}d} + \beta_{\mathbf{k}} n_{pd} n_d + \alpha_{\mathbf{k}} n_{pd}^e n_d + n_{pd} n_{pp}^e + n_{pd}^e n_{pp} \\
&\quad - 2t_{pd} (n_{ps} - \alpha_{\mathbf{k}} n_d n_{dd'}) - I^{11}(\mathbf{k}) + 2t_{pd} I^{12}(\mathbf{k}), \\
F_{tt}(\mathbf{k}) &= (2n_p U_p - e_d) X_{tt}(\mathbf{k}) - U_d (n_{\bar{d}d} + n_{\bar{p}c}) + \beta_{\mathbf{k}} |n_{pd}|^2 + \alpha_{\mathbf{k}} n_{dp} n_{pd}^e + 2n_{pp} n_{pp}^e \\
&\quad + 2t_{pd} [\alpha_{\mathbf{k}} n_{dp} (n_{dd'} - n_{pp}) + 3n_{pt} - n_{cd'}] + I^{13}(\mathbf{k}) - 2t_{pd} I^{14}(\mathbf{k}).
\end{aligned}$$

3. Integrals $I_m^1(\mathbf{k}), \dots, I^{14}(\mathbf{k})$

In the susceptibility and frequency matrix fourteen functions $I_m^1(\mathbf{k}), \dots, I^{14}(\mathbf{k})$ appear containing double integrations in reciprocal space. Their definitions are as follows:

$$\begin{aligned}
I_m^1(\mathbf{k}) &= \frac{1}{N} \sum_{\mathbf{q}} \epsilon_{m\mathbf{q}} D_m^1(\mathbf{k}-\mathbf{q}), & I_m^2(\mathbf{k}) &= \frac{1}{N} \sum_{\mathbf{q}} \phi_{m\mathbf{q}}^* D_m^2(\mathbf{k}-\mathbf{q}), \\
I^3(\mathbf{k}) &= \frac{1}{N} \sum_{\mathbf{q}} \alpha_{\mathbf{q}} D^3(\mathbf{k}-\mathbf{q}), & I_m^4(\mathbf{k}) &= \frac{1}{N} \sum_{n\mathbf{q}} \phi_{n\mathbf{q}}^* D_m^4(\mathbf{k}-\mathbf{q}) [\delta_{mn} - 2n_{mn}(\mathbf{q})], \\
I_m^5(\mathbf{k}) &= \frac{1}{N} \sum_{\mathbf{q}} \epsilon_{m\mathbf{q}} \phi_{m\mathbf{q}}^* D_m^2(\mathbf{q}-\mathbf{k}), & I^6(\mathbf{k}) &= \frac{1}{N} \sum_{m\mathbf{q}} \epsilon_{m\mathbf{q}} |\phi_{m\mathbf{q}}|^2 D^3(\mathbf{k}-\mathbf{q}), \\
I_m^7(\mathbf{k}) &= \frac{1}{N} \sum_{\mathbf{q}} \{n_{mp}(\mathbf{q}) D_m^9(\mathbf{q}-\mathbf{k}) + 2\phi_{m\mathbf{q}}^* n_{dp}(\mathbf{q}) D_m^4(\mathbf{q}-\mathbf{k}) + [\phi_{m\mathbf{q}}^* - 2n_{mp}(\mathbf{q})] D_m^7(\mathbf{q}-\mathbf{k})\}, \\
I^8(\mathbf{k}) &= \frac{1}{N} \sum_{\mathbf{q}} n_{dp}(\mathbf{q}) D^6(\mathbf{q}-\mathbf{k}), & I^9(\mathbf{k}) &= \frac{1}{N} \sum_{\mathbf{q}} \alpha_{\mathbf{q}} D^6(\mathbf{q}-\mathbf{k}), \\
I_m^{10}(\mathbf{k}) &= \frac{1}{N} \sum_{n\mathbf{q}} \phi_{n\mathbf{q}}^* (\delta_{mn} - 2n_{mn}) [\epsilon_{m\mathbf{q}} D_m^4(\mathbf{q}-\mathbf{k}) + D_m^5(\mathbf{q}-\mathbf{k})], \\
I^{11}(\mathbf{k}) &= \frac{1}{N} \sum_{m\mathbf{q}} \phi_{m\mathbf{q}} n_{md}(\mathbf{q}) [\epsilon_{m\mathbf{q}} D^6(\mathbf{q}-\mathbf{k}) + D^{10}(\mathbf{q}-\mathbf{k})], \\
I^{12}(\mathbf{k}) &= \frac{1}{N} \sum_{\mathbf{q}} \alpha_{\mathbf{q}} [1 - n_{33}(\mathbf{q})] D^6(\mathbf{q}-\mathbf{k}), \\
I^{13}(\mathbf{k}) &= \frac{1}{N} \sum_{mn\mathbf{q}} \phi_{m\mathbf{q}} \phi_{n\mathbf{q}}^* [\delta_{mn} - 2n_{mn}(\mathbf{q})] [\epsilon_{m\mathbf{q}} D^6(\mathbf{q}-\mathbf{k}) + D^{10}(\mathbf{q}-\mathbf{k})], \\
I^{14}(\mathbf{k}) &= \frac{1}{N} \sum_{\mathbf{q}} \{[\alpha_{\mathbf{q}} - n_{pp}(\mathbf{q})] D^8(\mathbf{q}-\mathbf{k}) + n_{pd'}(\mathbf{q}) D^6(\mathbf{q}-\mathbf{k})\}.
\end{aligned}$$

Thereby, the following abbreviations for functions including a single integration in reciprocal space have been used:

$$\begin{aligned}
D_m^1(\mathbf{k}) &= \frac{1}{N} \sum_{\mathbf{q}} n_{mm}(\mathbf{q}) n_{mm}(\mathbf{q}+\mathbf{k}), & D_m^2(\mathbf{k}) &= \frac{1}{N} \sum_{\mathbf{q}} n_{md}(\mathbf{q}) n_{dm}(\mathbf{q}+\mathbf{k}), \\
D^3(\mathbf{k}) &= \frac{1}{N} \sum_{\mathbf{q}} n_{dd}(\mathbf{q}) [1 - n_{dd}(\mathbf{q}+\mathbf{k})], & D_m^4(\mathbf{k}) &= \frac{1}{N} \sum_{\mathbf{q}} \phi_{m\mathbf{q}} n_{md}(\mathbf{q}+\mathbf{k}), \\
D_m^5(\mathbf{k}) &= \frac{1}{N} \sum_{\mathbf{q}} (\epsilon_{m\mathbf{q}} - \epsilon_{m(\mathbf{q}+\mathbf{k})}) \phi_{m\mathbf{q}} n_{md}(\mathbf{q}+\mathbf{k}), & D^6(\mathbf{k}) &= \frac{1}{N} \sum_{\mathbf{q}} \alpha_{\mathbf{q}} n_{dd}(\mathbf{q}+\mathbf{k}), \\
D_m^7(\mathbf{k}) &= \frac{1}{N} \sum_{\mathbf{q}} \phi_{m\mathbf{q}}^* \phi_{m(\mathbf{q}+\mathbf{k})} n_{dd}(\mathbf{q}+\mathbf{k}), & D^8(\mathbf{k}) &= \frac{1}{N} \sum_{\mathbf{q}} \alpha_{\mathbf{q}} n_{dp}(\mathbf{q}+\mathbf{k}), \\
D_m^9(\mathbf{k}) &= \frac{1}{N} \sum_{n\mathbf{q}} \phi_{m(\mathbf{q}+\mathbf{k})} \phi_{n\mathbf{q}}^* n_{mn}(\mathbf{q}), & D^{10}(\mathbf{k}) &= \frac{1}{N} \sum_{\mathbf{q}} \beta_{\mathbf{q}} n_{dd}(\mathbf{q}+\mathbf{k}).
\end{aligned}$$

4. Approximations

In many frequency and susceptibility matrix elements, expectation values of four fermion operators appear, which cannot be determined within the self-consistent scheme. These expressions are reduced to expectation values of two fermion operators by applying the Hartree-Fock approximation [see Eq. (25)]. In particular, all expressions generated by the oxygen-oxygen hopping t_{pp} have been evaluated in that way. Furthermore, in matrix elements of the oxygen operators A_p and $A_{\bar{p}}$ exclusively the Hartree-Fock approximation has been used.

The strong Coulomb terms proportional to U_d require approximations in the frequency matrix elements F_{ts} , F_{tc} , and F_{tt} . These static expressions, which are valid for the lattice, have been replaced by the corresponding terms for a single CuO_4 plaquette, which can be calculated self-consistently. Considering the local character of the Coulomb interaction in the Emery model this treatment is well justified.

A local approximation has also been chosen for several t_{pd} terms and for some expressions in the susceptibility matrix. This refers to the terms n_{pc} , n_{ds} , $n_d - n_{\bar{d}}$ in the susceptibility matrix elements X_{tt} , X_{ts} , X_{ss} , respectively, and to the t_{pd} terms n_{dc} , n_{ds} , $2n_{ps} - n_{cp} + n_{\bar{d}}$, n_{ps} , $3n_{pt} - n_{cd'}$, n_{ds} in the frequency matrix elements F_{ss} , $F_{t\bar{d}}$, F_{ts} , F_{tc} , F_{tt} , F_{cs} , respectively. The corresponding expectation values have been reduced to self-consistent occupation numbers by replacing a phase factor $|\phi_{m\mathbf{q}}|^2$ in the integrals for the lattice by its mean value 1. The omission of the phase factor, which corresponds to a local approximation of the expectation value, turns out to be a better approximation in these cases than the Hartree-Fock decoupling.

The validity of these approximations has been tested on a single CuO_4 plaquette. Additionally, one can compare the resulting spectra with exact diagonalizations of a 2×2 CuO_2 cluster (see Sec. V). In both cases the chosen approximations appear to be very reliable.

- ¹V. J. Emery, Phys. Rev. Lett. **58**, 2794 (1987).
²M. S. Hybertsen, M. Schlüter, and N. E. Christensen, Phys. Rev. B **39**, 9028 (1989).
³M. S. Hybertsen, E. B. Stechel, M. Schlüter, and D. R. Jennison, Phys. Rev. B **41**, 11 068 (1990).
⁴A. K. McMahan, R. M. Martin, S. Satpathy, Phys. Rev. B **38**, 6650 (1988).
⁵L. F. Mattheis, Phys. Rev. Lett. **58**, 1028 (1987).
⁶J. Yu, A. J. Freeman, J.-H. Xu, Phys. Rev. Lett. **58**, 1035 (1987).
⁷C. Mei and G. Stollhoff, Z. Phys. B **77**, 353 (1989).
⁸J. B. Grant and A. K. McMahan, Phys. Rev. **46**, 8440 (1992).
⁹P. Horsch and W. Stephan, in *Proceedings of the NATO Advanced Research Workshop on Interacting Electrons in Reduced Dimensions*, edited by D. Baeriswyl and D. Campbell, NATO ASI Series, Series B, Physics, Vol. 213 (Plenum, New York, 1989).
¹⁰P. Horsch and W. Stephan, in *Proceedings of the NATO Advanced Research Workshop on Dynamics of Magnetic Fluctuations in High-Temperature Superconductors*, edited by G. Reiter, P. Horsch, and G. C. Psaltakis, NATO ASI Series, Series B, Physics, Vol. 246 (Plenum, New York, 1991).
¹¹H. Eskes and G. A. Sawatzky, Phys. Rev. Lett. **61**, 1415 (1988).
¹²H. Eskes and G. A. Sawatzky, Phys. Rev. B **43**, 119 (1991).
¹³H. Eskes, M. B. Meinders, and G. A. Sawatzky, Phys. Rev. Lett. **67**, 1035 (1991); M. B. Meinders, H. Eskes, and G. A. Sawatzky, Phys. Rev. B **48**, 3916 (1993).
¹⁴A. Ramšak and P. Prelovšek, Phys. Rev. B **40**, 2239 (1989).
¹⁵H. J. Schmidt and Y. Kuramoto, Phys. Rev. B **42**, 2562 (1990).
¹⁶J. Wagner, W. Hanke, and D. J. Scalapino, Phys. Rev. B **43**, 10 517 (1991).
¹⁷T. Tohyama and S. Maekawa, Physica C **191**, 193 (1992).
¹⁸Y. Ohta, K. Tsutsui, W. Koshibae, T. Shimozato, and S. Maekawa, Phys. Rev. B **46**, 14 022 (1992).
¹⁹G. Dopf, A. Muramatsu, and W. Hanke, Phys. Rev. B **41**, 9264 (1990).
²⁰G. Dopf, J. Wagner, P. Dietrich, A. Muramatsu, and W. Hanke, Phys. Rev. Lett. **68**, 2082 (1992).
²¹R. T. Scalettar, D. J. Scalapino, R. L. Sugar, and S. R. White, Phys. Rev. B **44**, 770 (1991).
²²C. A. Balseiro, M. Avignon, A. G. Rojo, and B. Alascio, Phys. Rev. Lett. **62**, 2624 (1988).
²³G. Kotliar, P. A. Lee, and N. Read, Physica C **153-155**, 538 (1988).
²⁴C. A. R. Sá de Melo and S. Doniach, Phys. Rev. B **41**, 6633 (1990).
²⁵P. C. Pattnaik and D. M. Newns, Phys. Rev. B **41**, 880 (1990).
²⁶J. Brinkmann and N. Grewe, Z. Phys. B **84**, 179 (1991).
²⁷J. Schmalian, G. Baumgärtel, and K.-H. Bennemann, Phys. Rev. Lett. **68**, 1406 (1992).
²⁸H. Matsumoto, M. Sasaki, and M. Tachiki, Solid State Commun. **71**, 829 (1989).
²⁹H. Matsumoto, M. Sasaki, S. Ishihara, and M. Tachiki, Phys. Rev. B **46**, 3009 (1992); M. Sasaki, H. Matsumoto, and M. Tachiki, Phys. Rev. B **46**, 3022 (1992).
³⁰J. Zaanen and A. Oleś, Phys. Rev. B **37**, 9423 (1989).
³¹J. H. Jefferson, H. Eskes, and L. F. Feiner, Phys. Rev. B **45**, 7959 (1992).
³²R. Hayn, V. Yushankhai, and S. Lovtsov, Phys. Rev. B **47**, 5253 (1993).
³³F. C. Zhang and T. M. Rice, Phys. Rev. B **37**, 3759 (1987).
³⁴K. W. Becker, W. Brenig, and P. Fulde, Z. Phys. B **81**, 165 (1990).
³⁵R. Hayn, V. Yushankhai, Phys. Status Solidi B **166**, 415 (1991).
³⁶A. J. Fedro, Yu Zhou, T. C. Leung, B. N. Harmon, and S. K. Sinha, Phys. Rev. B **46**, 14 785 (1992).
³⁷P. Unger and P. Fulde, Phys. Rev. B **47**, 8947 (1993).
³⁸J.-M. Imer, F. Patthey, B. Dardel, W.-D. Schneider, Y. Baer, Y. Petroff, and A. Zettl, Phys. Rev. Lett. **62**, 336 (1989).
³⁹G. Mante, R. Claessen, T. Buslaps, S. Harm, R. Manzke, M. Skibowski, and J. Fink, Z. Phys. B **80**, 181 (1990).
⁴⁰R. Manzke, T. Buslaps, R. Claessen, M. Skibowski, and J. Fink, Physica C **162-164**, 1381 (1989).
⁴¹J. Fink, N. Nücker, H. Romberg, M. Alexander, and

- P. Adelman, R. Claessen, G. Mante, T. Buslaps, S. Harm, R. Mancke, and M. Skibowsky, in *Highlights in Condensed Matter Physics and Future Prospects*, edited by L. Esaki (Plenum, New York, 1991).
- ⁴²B. W. Veal, J. Z. Liu, A. P. Paulikas, K. Vandervoort, H. Claus, J. C. Campuzano, C. Olson, A.-B. Yang, R. Liu, C. Gu, R. S. List, A. J. Arko, and R. Bartlett, *Physica C* **158**, 276 (1989).
- ⁴³H. Romberg, M. Alexander, N. Nücker, P. Adelman, and J. Fink, *Phys. Rev. B* **42**, 8768 (1990).
- ⁴⁴C. T. Chen, F. Sette, Y. Ma, M. S. Hybertsen, E. B. Stechel, W. M. C. Foulkes, M. Schlüter, S.-W. Cheong, A. S. Cooper, L. W. Rupp, Jr., B. Batlogg, Y. L. Soo, Z. H. Ming, A. Krol, and Y. H. Kao, *Phys. Rev. Lett.* **66**, 104 (1991).
- ⁴⁵T. Takahashi, H. Matsuyama, H. Katayama-Yoshida, Y. Okabe, S. Hosoya, K. Seki, H. Fujimoto, M. Sato, and H. Inokuchi, *Phys. Rev. B* **39**, 6636 (1989).
- ⁴⁶C. G. Olson, R. Liu, D. W. Lynch, R. S. List, A. J. Arko, B. W. Veal, Y. C. Chang, P. Z. Jiang, and A. P. Paulikas, *Phys. Rev. B* **42**, 381 (1989).
- ⁴⁷J. C. Campuzano, L. C. Smedskjaer, R. Benedek, G. Jennings, and A. Bansil, *Phys. Rev. B* **43**, 2788 (1990).
- ⁴⁸J. M. Luttinger, *Phys. Rev.* **119**, 1153 (1960).
- ⁴⁹R. Zwanzig, *Lectures in Theoretical Physics* (Interscience, New York, 1961), Vol. 3; H. Mori, *Progr. Theor. Phys.* (Kyoto) **34**, 423 (1965).
- ⁵⁰K. W. Becker and P. Fulde, *Z. Phys. B* **72**, 423 (1988); K. W. Becker and W. Brenig, *ibid.* **79**, 195 (1990).
- ⁵¹F. Forster, *Hydrodynamic Fluctuations, Broken Symmetry and Correlation Functions* (Benjamin, New York, 1975).
- ⁵²J. Hubbard, *Proc. R. Soc. London Ser. A* **276**, 238 (1963).
- ⁵³A. J. Fedro and S. K. Sinha, *Valence Instabilities*, edited by P. Wachter and H. Boppert (North-Holland, Amsterdam, 1982).
- ⁵⁴P. Horsch and W. Stephan (private communication).
- ⁵⁵M. A. van Veenendaal, R. Schlatmann, G. A. Sawatzky, and W. A. Groen, *Phys. Rev. B* **47**, 446 (1993).
- ⁵⁶N. P. Ong, Z. Z. Wang, J. Clayhold, J. M. Tarascon, L. H. Greene, and W. R. McKinnon, *Phys. Rev. B* **35**, 8807 (1987).
- ⁵⁷M. Suzuki, *Phys. Rev. B* **39**, 2312 (1989).
- ⁵⁸S. Uchida, T. Ido, H. Takagi, T. Arima, Y. Tokura, and S. Tajima, *Phys. Rev. B* **43**, 7942 (1991).
- ⁵⁹L. D. Rotter, Z. Schlesinger, R. T. Collins, F. Hotzberg, C. Field, U. W. Welp, G. W. Crabtree, J. Z. Liu, Y. Fang, K. G. Vandervoort, and S. Fleshler, *Phys. Rev. Lett.* **67**, 2741 (1991).